

Aristotle University of Thessaloniki
Faculty of Engineering
School of Electrical and Computer Engineering
Department of Telecommunications



Marios Palaskos (8492)

DIPLOMA THESIS

Low complexity receivers in simultaneous wireless information and power
transfer MISO systems

Supervisor: Pr. George Karagiannidis

Thessaloniki, October 2020

© Marios Palaskos

© Α.Π.Θ.

Low complexity receivers in simultaneous wireless information and power transfer MISO systems

«Η έγκριση της παρούσης διπλωματικής εργασίας από το Τμήμα Ηλεκτρολόγων Μηχανικών και Μηχανικών Υπολογιστών του Αριστοτελείου Πανεπιστημίου Θεσσαλονίκης δεν υποδηλώνει αποδοχή των γνώμων του συγγραφέως»

(Ν. 5343/1932, άρθρο 202, παρ. 2)

To those seeking after truth

Abstract

In today's widely used devices and internet-of-things (IoT) applications, such sensor networks, which require connection to the power cord, energy harvesting (EH) from sources that intentionally generate radio frequency (RF) signals can prolong the lifetime of the utilized devices. The potential to use this concept, termed as wireless power transfer (WPT), in communication applications, has received much attention recently. However, WPT complicates the design of communication systems, since, in some cases, it conflicts with the wireless information transmission (WIT). More specifically, nodes cannot harvest energy and receive information simultaneously. This is the main challenge of simultaneous wireless information and power transfer (SWIPT), which aims at unifying the information and energy transmission. To achieve this, the received signal has to be split in two distinct parts, one for energy harvesting and one for information decoding (ID). The time-switching (TS) scheme achieves SWIPT by dividing each transmission block into two orthogonal time slots, one for transferring power and the other for transmitting data, while the power-splitting (PS) scheme uses a PS component that splits the received signal into two streams of different power levels. In the separated receiver architecture, the ID and EH receivers consist of the traditional circuits used for information processing and energy harvesting respectively and the splitting technique is employed at the RF-band. In the integrated receiver architecture, both procedures are performed by the same circuit, which is conventionally used only for EH, thereby reducing the energy cost significantly, and the splitting protocol is employed at the baseband. This Diploma Thesis studies a multiple-input single-output (MISO) transmission system, which consists of a multi-antenna base station transmitting information and energy simultaneously to a single-antenna user that uses the integrated receiver architecture. The MISO-SWIPT system model is presented and the expression of the received signal is derived. Assuming channel state information (CSI) at the transmitter, beamforming is employed by the transmitter, so that the maximum harvested energy is achieved at the receiver. In this case, the optical intensity channel with peak and average power constraints that emerges is addressed using existing research findings, which are summarized and further analyzed. In particular, the rate is derived using a capacity approaching distribution, which reduces the complexity, and along with an expression for the harvested energy are used to study the effect of the number of the transmitting antennas on the achievable rate-energy region. Finally, the optimal splitting factors are computed by minimizing the maximum value of the outage probability of the system, testing its performance with simulations.

Keywords: Telecommunications, simultaneous wireless information and power transfer (SWIPT), integrated receiver, optical intensity channel, rate-energy region, outage probability

Acknowledgements

Firstly, I am deeply indebted to my supervisor Pr. George Karagiannidis for giving me the opportunity to do research in a subject suitable for my academic interests, which helped me expand my theoretical knowledge in telecommunications and hone my programming skills.

During my thesis I also had great pleasure working with PhD student Sotiris Tegos, whose apt observations on my dissertation proved conducive to my carrying through with the project. I gratefully acknowledge the assistance of Pr. Leonidas Georgiadis in clarifying concepts of the optical intensity channel for me.

Nevertheless, I cannot leave university without mentioning my family and friends, who have been my bulwarks during my studies. For this reason I would like to express my deepest and sincere gratitude to my family for their unconditional love, implicit support and sacrifices for educating and preparing me for my future, as well as to my friends for their practical suggestions and profound belief in my abilities, which encouraged me to surmount the obstacles I encountered.

Contents

Abstract	i
Acknowledgements	ii
Contents	iii
List of Figures	iv
1 Introduction	1
1.1 Historical Frame/Purpose	1
1.1.1 Fifth Generation Communication Networks (5G)	1
1.1.2 SWIPT in 5G networks	3
1.2 Bibliography	4
1.3 Contribution	5
1.4 Structure/Notation	6
2 System Analysis	7
2.1 System model	7
2.2 Architecture for the integrated information and energy receiver	9
2.3 Energy harvesting and information decoding	11
2.4 Fading channel and path loss factor modeling	16
3 System performance evaluation	18
3.1 Optical intensity channel with peak and average power constraints	18
3.1.1 Bounds on channel capacity	19
3.1.2 Channel capacity approximation	24
3.2 Energy harvesting models	29
3.3 System performance metrics	30
3.3.1 Rate-Energy region	31
3.3.2 Joint rate-energy outage probability	32
4 Numerical results and discussion	37
4.1 Simulations	37
4.2 Conclusions	44
References	46

List of Figures

1.1	5G network architecture	1
1.2	SWIPT in 5G networks	2
2.1	System model	7
2.2	Architecture for the integrated information and energy receiver	9
2.3	Architecture for the integrated receiver with DPS	10
2.4	Architecture for the integrated receiver with SPS	10
2.5	Architecture for the integrated receiver with TS	11
3.1	The graph of the function $v(r)$	23
3.2	Upper and lower bounds on capacity for $r = 2$ and $r = 6$	24
3.3	Upper and lower bounds on capacity along with the mutual information that approaches the capacity	28
3.4	The mutual information that approaches the channel capacity versus SNR	28
3.5	The nonlinear EH model (3.45) for $P_S = 0.024$, $A = 150$, $B = 0.014$ versus the average input power (the graph at the top of the figure). A comparison between the linear EH model with $\zeta = 0.78$ and the nonlinear EH model with $P_S = 0.024$, $A = 150$, $B = 0.014$ (the graph at the bottom of the figure).	30
4.1	Rate-energy tradeoff in a $n_T \times 1$ MISO PS system, where $n_T = 1, 2, 4$	38
4.2	Rate-energy tradeoff in a $n_T \times 1$ MISO TS system, where $n_T = 1, 2, 4$	38
4.3	A comparison between the R-E regions of the PS and TS schemes for $\frac{LP}{\sigma} = 3 \text{ dB}$ (the graph at the top of the figure) and $\frac{LP}{\sigma} = 10 \text{ dB}$ (the graph at the bottom of the figure), where $n_T = 1$	39
4.4	Optimal splitting factors ρ^* (PS scheme), a^* (TS scheme) versus the peak-to-average power ratio r	40
4.5	Optimal PS factor ρ^* versus energy and rate thresholds.	41
4.6	Optimal TS factor a^* versus energy and rate thresholds.	41
4.7	Outage probability versus BS-receiver distance for PS and TS schemes in a $n_T \times 1$ MISO system, where $n_T \in \{1, 2, 4\}$	42
4.8	Outage probability versus LP/σ for PS and TS schemes in a $n_T \times 1$ MISO system, where $n_T \in \{1, 2, 4\}$	42
4.9	Outage probability versus r for PS and TS schemes in a $n_T \times 1$ MISO system, where $n_T \in \{1, 2, 4\}$	43

4.10 Outage probability versus r_{th} and q_{th} for PS scheme, where the BS has $n_T = 4$ antennas.	43
4.11 Outage probability versus r_{th} and q_{th} for TS scheme, where the BS has $n_T = 4$ antennas.	44

Chapter 1

Introduction

1.1 Historical Frame/Purpose

1.1.1 Fifth Generation Communication Networks (5G)

Mobile communications have played an integral part in shaping our society, connecting us with people across the world and helping us carry out many daily tasks. Cellular technologies have evolved from 1G in 1982 to 4G in 2010 (with a time interval of 10 years between two consecutive generations) with various points of focus like data rate, energy dissipation, bandwidth utilization, and spectrum management. However, as more people are dragged into the world of the internet, spectrum bands used by prevalent 4G networks are becoming congested, leading to server crashes. Industry forecasts predict that the number of internet-connected devices will exceed 25 billion by 2025, whilst the number of mobile subscribers will exceed 7 billion by the same year. To that end, the Fifth Generation mobile network (5G) has been designed to meet the very large growth in data and connectivity of today's modern society, thereby supporting the massive number of devices, which have a diverse range of speed, bandwidth and quality of service requirements. All in all, as illustrated in Figure 1.1, 5G will enable instantaneous connectivity to billions of devices, the Internet of Things (IoT) and a truly connected world, without human intervention at a scale not seen before.

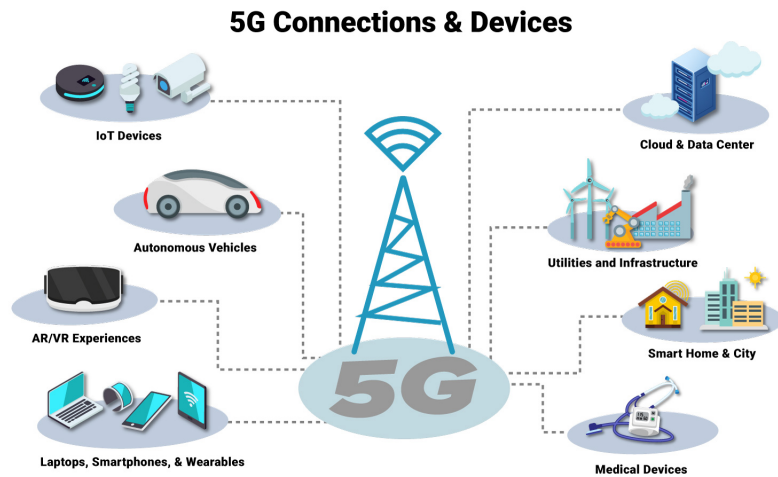


Figure 1.1: 5G network architecture

Upgrading the quality-of-service (QoS) of subscribers along with the quality-of-experience (QoE) is a major concern in 5G wireless networks. Along with the existing LTE frequency range, the 5G network spectrum also includes the millimeter-wave band. This network using a high spectrum paired with an advanced radio technology is expected to deliver up to 100 times faster connections (faster speeds in data access, downloading and streaming content) and greater capacity, which enables more people and more devices to communicate with each other simultaneously. A very important advantage of 5G is the fast response time referred to as latency, meaning that devices will enjoy virtually instantaneous connections to the network (the delay time is around 5ms and can be reduced to 1ms, almost 10 times less than the latency of 4G technology). These features of 5G increase the chances of the establishment of smart cities, that regulate themselves using various sensor connections and have the potential to revolutionize modern industrial processes and applications including agriculture, manufacturing and business communications. Low latency communications also open up a new world where remote medical care, procedures, and treatment are all possible.

However, introducing 5G technology to the world inevitably leads to increased consumption of time and money. On the one hand, this is because the existing mobile infrastructures that are not compatible with 5G technology need to be replaced. On the other hand, telecommunications service suppliers have to increase the antennas of their network so that the coverage remains the same as in 4G technology. In particular, the total coverage provided by each cell of 5G networks will decrease, as a result of an increase in bandwidth. An additional factor is the fact that, millimeter waves, generally, have very low penetrating power and cannot pass through buildings, trees, walls or other barriers without the signal being disrupted. Apart from the financial ramifications of the new technology, the significant increase in data speed and connectivity will bring about equally large energy consumption, which degrades the QoE of the users with battery powered devices, because batteries have a limited operating time. Addressing this issue will become more difficult, as the power consumed by our modern communication network will increase due to the proliferation of the number of internet-connected devices, which is set to explode even further with the coming of the IoT. To that end, simultaneous wireless information and power transfer (SWIPT) is an interesting new area of research that has attracted increasing attention by academia and industry.

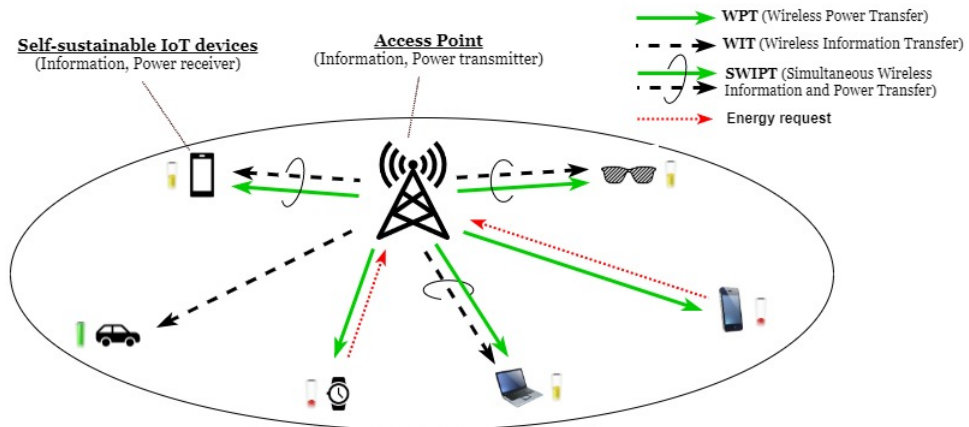


Figure 1.2: SWIPT in 5G networks

1.1.2 SWIPT in 5G networks

Whilst recharging the batteries can extend the lifetime of the network to a certain extent, it usually experiences high costs and cannot meet the mobility and autonomy demands of the users. In addition to that, it may not be very convenient in certain cases like toxic environments or inside human bodies, etc. As a sustainable solution to prolong the lifetime of energy-constrained wireless networks, energy harvesting (EH) technique has recently drawn significant attention.

EH is a process of capturing and converting wasted or unimportant energy such as heat, sound and Radio Frequency (3kHz-300GHz) signals into electricity and putting it to work based on power requirements. The ambient environment contains high-quality energy sources compared to currently available batteries and charged super-capacitors. Lately, several studies have explored the possibility of using the conventional renewable sources, such as solar and wind, in the EH process within the communications network. They were proved, though, not as effective as expected due to their irregular and unforeseeable nature. However, the level of the ambient RF signals is unceasingly growing because of wireless systems such as mobile base stations, Wi-Fi applications, TV and radio base stations, wireless routers and other systems that exploit wireless networks. Wireless Power Transfer (WPT) is one of the EH technologies that overcome the above limitations, since it is less dependent on weather circumstances. The rapid advancement of the technology facilitates WPT, for the wireless transceivers and sensors are becoming smaller in size and more power efficient (with a power consumption that is in order of a Watt or less).

WPT is an innovative concept for use of electricity that was originally devised by Nikola Tesla in the 1890s. WPT refers to the transmission of electrical energy from a power source by means of electromagnetic fields, to an electrical component or a portion of a circuit that consumes electrical power without the aid of wired interconnections. The WPT system contains a transmitter connected to the main power source, which transforms main power to a time variant electromagnetic field, and one or more receiver devices to receive and harvest energy from the electromagnetic field. Two factors, long-distance transmission and high power, have been more focused during early efforts on WPT. Nevertheless, the low efficiency of the transmission process and the health concerns for such high-power applications prevented their further development. Therefore, most WPT research continued in two distinct regions, non-radiative (near field) and radiative (far field). In the non-radiative technique, power is transferred by magnetic fields through the inductive coupling (for charging mobile phones, medical implants, and electrical vehicles). In the radiative technique, power is transferred by a beam of electromagnetic radiation. Different WPT technologies differ in terms of the range in which they can transfer power efficiently.

Since RF signals can carry energy and information at the same time, we envision that radio waves will not only become a major source of power for operating wireless devices, but also their information and power transmission aspects will be unified. A proper design that considers both information and power can provide noteworthy energy efficient wireless communication and lead to possible state-of-the-art applications and services for the 5G, laying the foundations of the next-generation sustainable societies. For instance, wireless implants can be charged and calibrated concurrently with the same signal. Healthcare will also improve, as the collated information can be obtained from multiple sources of data very quickly and thereby leading

to quick decisions. SWIPT could be the only option to deploy nodes at remote locations as well as in industrial applications. Therefore, how to deal with the contradiction between energy conservation and rate improvement has become a prominent issue in the design and optimization of 5G wireless networks (Figure 1.2).

1.2 Bibliography

As discussed in the previous section, background radio-frequency (RF) signals radiated by ambient transmitters can be a viable new source for wireless power transfer (WPT). The maximum theoretical power available for RF energy harvesting is 7 μ W and 1 μ W for 2.4 GHz and 900 MHz frequency, respectively, for free space distance of 40 m [1]. On the other hand, RF signals have been widely used as a vehicle for wireless information transmission (WIT). Simultaneous wireless information and power transfer (SWIPT) becomes appealing since it realizes both useful utilizations of RF signals at the same time, and thus potentially offers great convenience to mobile users.

SWIPT was first studied in a point-to-point single-antenna additive white Gaussian noise (AWGN) channel from an information-theoretic standpoint [2]. This work was extended in [3] to frequency-selective single-antenna AWGN channels, where nontrivial tradeoff between information rate and harvested energy was demonstrated by varying power allocation over frequency. A similar trade-off was derived for a multi-user system in [4]. The aforementioned works implicitly assumed that the receiver is able to decode the information and harvest the energy from the same signal, which is infeasible given the current state-of-the-art of electronic circuits. This motivated the design of practical SWIPT-enabled receivers that split the received signal from each antenna and feed it to two separate circuits, one for information decoding and one for energy harvesting [5].

The authors in [6] studied SWIPT for fading AWGN channels subject to time-varying co-channel interference and proposed a new principle termed “opportunistic energy harvesting”, where the receiver switches between harvesting energy and decoding information based on the wireless channel condition and interference power level. Another key concern for SWIPT is drastically decaying power transfer efficiency with the increasing transmission distance due to propagation path loss. To tackle this problem, multiple-input multiple-output (MIMO) techniques were investigated to significantly improve the power transfer efficiency while still achieving high spectral efficiency for information transmission [7–12]. In [7], Zhang and Ho first investigated SWIPT for the MIMO broadcast channel with a multi-antenna transmitter sending information and energy simultaneously to one pair of energy receiver and information receiver, each with single or multiple antennas. Under two practical setups where information and energy receivers are either separated or co-located, the optimal precoder designs were developed to achieve different tradeoffs for maximal information rate versus energy transfer, which are characterized by the boundary of a so-called rate-energy (R-E) region. For the co-located receiver two practical designs were investigated, namely time-switching and power-splitting. The study in [7] was also extended to the cases with imperfect channel state information (CSI) at the transmitter in [8] and with non-linear energy harvested model in [9].

However, finding the optimal tradeoff between information rate and energy transfer does not constitute the only challenge of SWIPT systems. In particular, the conventional information receiver architecture designed for WIT may not be optimal for simultaneous information and power transfer, since in practice information and energy receivers have different power sensitivity (e.g., -60dBm for the information receiver versus -10dBm for the energy receiver). Therefore, the receiver architecture of a system that involves both WIT and WPT should be optimized for WPT. To that end, a novel integrated receiver architecture for SWIPT was proposed in [13], where the circuit for radio frequency to baseband conversion in the conventional information receiver is integrated to the front end of energy receiver via a rectifier, thus achieving energy saving. The integrated receiver has drawn much attention recently [14, 15].

Multiuser scenarios with dedicated information for each of the receivers have also been considered in the existing literature [16, 17]. However, in many practical communication systems, one transmitter needs to send a common message to a group of receivers simultaneously. These systems, which are referred to as multicasting systems, triggered great research interest [18, 19] due to the increasing demand for mobile applications such as streaming media, software updates, and location-based services involving group communications. The idea of SWIPT has also been studied in various case studies, such as orthogonal frequency division multiple access (OFDMA) [20–22], non-orthogonal multiple access (NOMA) [23, 24], and cooperative networks [25–28]. Finally, unlike the works on SWIPT that focused on the simultaneous energy and information transmissions to users in the downlink (DL), the authors in [29] propose an alternative setup where the hybrid access point (H-AP) broadcasts only wireless energy to users in the DL and then the users transmit their independent information using their individually harvested energy to the H-AP in the uplink (UL) by time-division-multiple-access (TDMA), a protocol termed “harvest-then-transmit”.

1.3 Contribution

This Diploma Thesis studies a multiple-input single-output (MISO) transmission system, which consists of a multi-antenna basestation (BS) sending information and energy simultaneously to a single-antenna user that uses the integrated receiver architecture. In the first place, the MISO-SWIPT system model is presented and the received signal is derived. Assuming channel state information (CSI) at the transmitter, beamforming is employed by the transmitter, so that the maximum harvested power is achieved at the receiver. In this case, the optical intensity channel with peak and average power constraints that emerges is addressed using existing research findings, which are summarized and further analyzed. The rate of the channel is approximated using a capacity-approaching distribution, which reduces the complexity of the problem, since mutual information depends on numerical computation of the output entropy. The rate along with the expression for the nonlinear harvesting model are used to display the achievable rate-energy region. Finally, the power splitting factor is derived by minimizing the maximum value of the outage probability of the system.

1.4 Structure/Notation

The rest of the thesis follows the structure as detailed below. Chapter 2 is devoted to thorough analysis of the MISO-SWIPT system: it presents the system mode, the possible receiver operation schemes as well as the energy harvesting and information decoding procedures. Chapter 3 addresses the optical intensity channel with peak and average power constraints and describes the energy harvesting models that are widely used. Subsequently, the achievable rate-energy region and the joint rate-energy outage probability of the system are examined. Chapter 4 evaluates the performance of the system using extensive simulation results and raises issues for further research.

Notation: $\mathbb{C}^{n \times m}$ denotes the space of $n \times m$ matrices with complex entries. Bold capital and lowercase letters represent matrices and vectors respectively, i.e. $\mathbf{\Sigma} \in \mathbb{C}^{n \times m}$, $\mathbf{A} \in \mathbb{C}^{n \times n}$, $\mathbf{x} \in \mathbb{C}^{n \times 1}$. For a square matrix \mathbf{A} , $\text{tr}(\mathbf{A})$ and \mathbf{A}^H denote its trace, conjugate transpose, while $\mathbf{A} \succeq 0$ means that it is positive semi-definite. $\text{diag}(x_1, \dots, x_N)$ denotes a $N \times N$ diagonal matrix with x_1, \dots, x_N being the diagonal elements. $\Re\{\cdot\}$ denotes the real part of a complex number, whereas $|\cdot|$, $\mathbb{E}[\cdot]$ and $\lfloor \cdot \rfloor$ denote the absolute value, the statistical expectation and the floor operation, respectively. To distinguish the density function of a random variable (RV) from the function of a scalar variable, for the former the random variable is used as the density function's name subscript. For example $f(x)$ is a function of the variable x , while $f_x(x)$ is the density function of the random variable X . $\mathcal{N}(\mu, \sigma^2)$, $\mathcal{CN}(\mu, \sigma^2)$ denote the normal distribution and complex normal distribution with mean value μ and standard deviation respectively. We use the symbol \sim to denote that a random variable follows a known distribution, i.e. $Z \sim \mathcal{N}(\mu, \sigma^2)$. As far as the information theory notation is concerned, $I(X; Y)$ denotes the mutual information of a channel with an input-output pair of random variables (X, Y) , while $H(X)$, $H_e(X)$ denote the entropy of the random variable X based on the binary logarithm $\log_2(\cdot)$ and natural logarithm $\log(\cdot)$, respectively.

Chapter 2

System Analysis

This chapter analyzes a multiple input-multiple output SWIPT system and presents the architecture of the integrated receiver along with its possible operation schemes. After the expression of the baseband signal at the receiver is derived, it is shown that beamforming has to be employed by the transmitter for the maximum harvested energy to be achieved at the receiver. The data rate is thus determined by the capacity of the optical intensity channel. In the last section the fading channel model is presented.

2.1 System model

The authors in [13] studied a point-to-point wireless link with simultaneous information and power transfer, where both the transmitter and the receiver are equipped with one single antenna. This chapter broadens this theoretical analysis to consider a similar system where only the transmitter is equipped with a finite number of antennas (Figure 2.1).

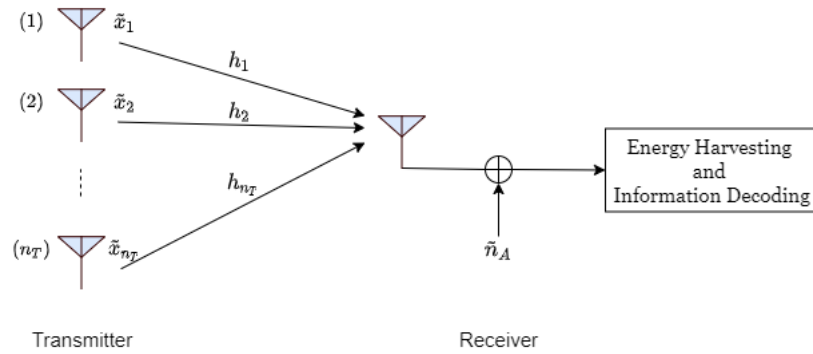


Figure 2.1: System model

Transmitter

We denote the complex baseband signal as $\mathbf{x}(t) \in \mathbb{C}^{n_T \times 1}$. Assuming that the baseband signal of each antenna is a narrow-band signal with bandwidth of B Hz, it is expressed as:

$$x_i(t) = A_i(t)e^{j\phi_i(t)}, \quad i \in \{1, \dots, n_T\} \quad (2.1)$$

where $A_i(t)$ and $\phi_i(t)$ denote the amplitude and phase of the complex baseband signal of the

i th antenna, while the transmitted RF band signal of each antenna is written as:

$$\tilde{x}_i(t) = \sqrt{2}A_i(t) \cos(2\pi f_c t + \phi_i(t)) = \sqrt{2} \Re\{x_i(t)e^{j2\pi f_c t}\}, \quad i \in \{1, \dots, n_T\} \quad (2.2)$$

It is also assumed that $B \ll f_c$ and the average transmit power is upper-bounded by P , i.e.:

$$\sum_{i=1}^{n_T} \mathbb{E}[\tilde{x}_i^2(t)] = \sum_{i=1}^{n_T} \mathbb{E}[A_i^2(t)] = \sum_{i=1}^{n_T} \mathbb{E}[|x_i(t)|^2] = \text{tr}(\mathbf{S}_{xx}) \leq P \quad (2.3)$$

where $\mathbf{S}_{xx} \in \mathbb{C}^{n_T \times n_T}$ denotes the autocorrelation matrix of the complex baseband signal, which is identical to:

$$\mathbf{S}_{xx} = \mathbb{E}[\mathbf{x}(t)\mathbf{x}^H(t)], \quad \mathbf{S}_{xx} \succeq 0 \quad (2.4)$$

Channel

Each transmitted signal propagates through a wireless channel with channel gain $|h_i| > 0$ and phase shift $\theta_i \in (0, 2\pi]$. Thus, the equivalent complex channel is expressed as $h_i = |h_i|e^{j\theta_i}$, $i \in \{1, \dots, n_T\}$.

Noise

The noise \tilde{n}_A introduced by the receiving antenna can be modeled as a narrow-band Gaussian noise with bandwidth B and center frequency f_c , i.e.:

$$\tilde{n}_A(t) = \sqrt{2} \Re\{n_A(t)e^{j2\pi f_c t}\} \quad (2.5)$$

where

$$n_A(t) = n_I(t) + jn_Q(t) \quad (2.6)$$

with $n_I(t), n_Q(t)$ denoting the in-phase and quadrature noise components, respectively. We assume that $n_I(t)$ and $n_Q(t)$ are independent Gaussian random variables with zero mean and variance $\sigma_A^2/2$, denoted by $\mathcal{N}(0, \sigma_A^2/2)$, where $\sigma_A^2 = N_0 B$, and N_0 is the one-sided noise power spectral density. Hence, we have $n_A \sim \mathcal{CN}(0, \sigma_A^2)$.

Receiver

Assuming a path loss factor L between the base station and the receiver, the signal arriving at the receiver, corrupted by the antenna noise, is given by:

$$y(t) = \sqrt{2} \left(\sqrt{L} \sum_{i=1}^{n_T} |h_i| A_i(t) \cos(2\pi f_c t + \phi_i(t) + \theta_i) + \tilde{n}_A(t) \right) \quad (2.7)$$

2.2 Architecture for the integrated information and energy receiver

Considering that the active mixers used in conventional information receiver for RF to baseband conversion are substantially power-consuming, the receiver that we examine in this thesis uses a passive rectifier operation, which is conventionally used only for energy harvesting, for both energy harvesting and information decoding. Therefore, the integrated receiver, as it is called, reduces the complexity of the system, since the net harvested energy that can be stored in the battery for future use increases, resulting in increase of the autonomy.

The architecture of the integrated receiver is illustrated in Figure 2.2. The received RF band signal $y(t)$ is converted to a direct current (DC) signal $i_{DC}(t)$ by a rectifier, which consists of a Schottky diode and a passive low-pass filter (LPF). In this case, the RF to direct current conversion is analogous to the RF to baseband conversion of the received signal in traditional wireless information receiver. Hence, the direct current is not only used to charge the battery to store the energy, but it can also be treated as a baseband signal for information decoding.

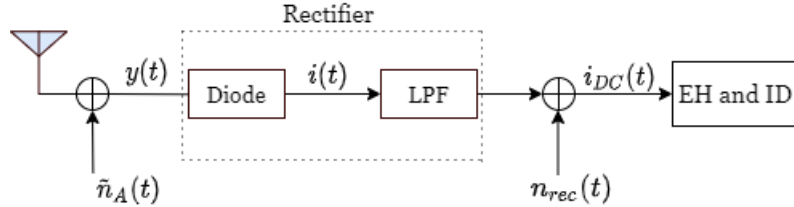


Figure 2.2: Architecture for the integrated information and energy receiver

Since the transmitted power in a wireless power transfer system can be varied over time provided that the average power delivered to the receiver is above a certain required target, we can encode information in the energy signal by varying its power levels over time, thus achieving continuous information transfer without degrading the power transfer efficiency. To emphasize this dual use of signal power in both WPT as well as WIT, the modulation scheme is called energy modulation. To decode the energy modulated information at the receiver, we need to detect the power variation in the received signal within a certain accuracy, by applying techniques such as energy detection.

However, currently available circuits that harvest energy from radio signal are not yet able to decode the carried information directly. In other words, the signal $i_{DC}(t)$ cannot be used for energy harvesting and information decoding at the same time. Due to this potential limitation, a practical Dynamic Power Splitting (DPS) scheme is proposed in [13] to enable the receiver to harvest energy and decode information from $i_{DC}(t)$ at any time t , by dynamically splitting the signal into two streams with power ratio $\rho(t) : 1 - \rho(t)$, which are used for harvesting energy and decoding information, respectively, where $0 \leq \rho(t) \leq 1$ (Figure 2.3). It is assumed that the power splitter is ideal, that is, it operates without any power loss or noise introduced, and that the receiver can perfectly synchronize its operations.

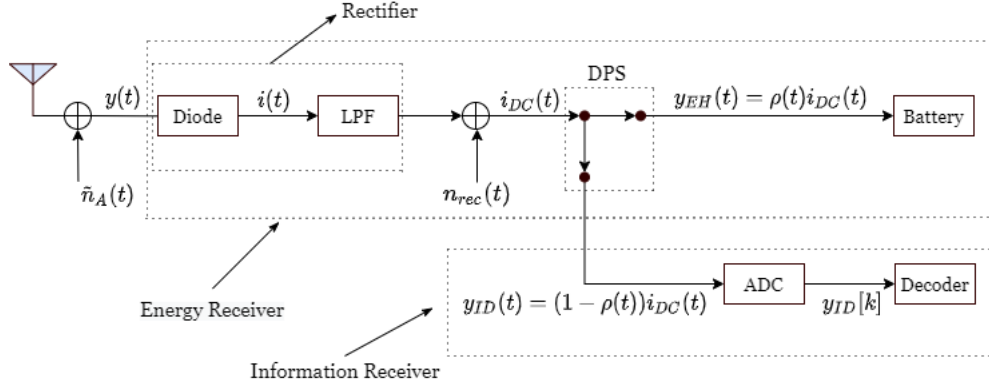


Figure 2.3: Architecture for the integrated receiver with DPS

Consider the case of N symbols (with period T_s each) being transmitted over a period of time T , i.e., $T = NT_s$, where it is assumed that $\rho(t) = \rho_k, \forall t \in [(k-1)T_s, kT_s), k = 1, \dots, N$. During the transmission block time T the information receiver may operate in two modes: switch off (off-mode) for a time duration T_{off} to save power, or switch on (on-mode) for a time duration $T_{on} = 1 - T_{off}$ to decode information. The percentage of time that the information decoder operates in off-mode is denoted by α with $0 \leq \alpha \leq 1$, thus we have $T_{off} = \alpha T$ and $T_{on} = (1 - \alpha)T$. Without loss of generality, it is assumed that the information receiver operates in off-mode during the first $\lfloor \alpha N \rfloor$ symbols in each block with $k = 1, \dots, \lfloor \alpha N \rfloor$, while in on-mode during the remaining symbols with $k = \lfloor \alpha N \rfloor + 1, \dots, N$. Since N is chosen to be a very large number in practice, αN can be approximated with a positive integer regardless of the value of α .

Next, three special cases of DPS are presented, namely *static power splitting* (SPS), *time switching* (TS) and *on-off power splitting* (OPS).

- *Static power splitting (SPS)*: With SPS, the information receiver operates in on-mode for all N symbols (i.e. $\alpha = 0$), and the ratio of the split signal power for harvesting energy and decoding information is set to be constant ρ for all N symbols. Thus for SPS, we have:

$$\rho_k = \rho, \quad k = 1, \dots, N \quad (2.8)$$

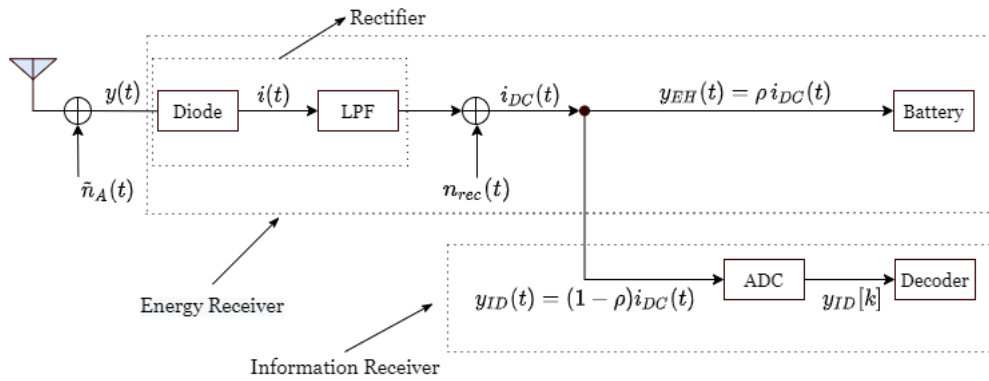


Figure 2.4: Architecture for the integrated receiver with SPS

- *Time switching (TS)*: With TS, for the first αN symbols when the information receiver operates in off-mode, all signal power is used for energy harvesting. For the remaining $(1 - \alpha)N$ symbols when the information receiver is on-mode, all signal power is used for energy harvesting. Thus for TS, we have:

$$\rho_k = \begin{cases} 1, & k = 1, \dots, \alpha N \\ 0, & k = \alpha N + 1, \dots, N \end{cases} \quad (2.9)$$

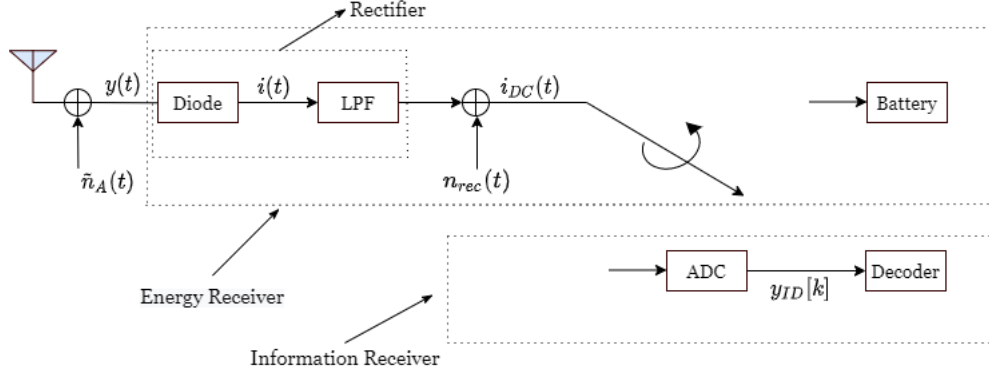


Figure 2.5: Architecture for the integrated receiver with TS

- *On-off power splitting (OPS)*: With OPS, for the first αN symbols all signal power is used for energy harvesting. For the remaining $(1 - \alpha)N$ symbols, the ratio of the split signal power for harvesting energy and decoding information is set to be constant ρ , with $0 \leq \rho < 1$. Thus, for a given power splitting pair (α, ρ) , we have:

$$\rho_k = \begin{cases} 1, & k = 1, \dots, \alpha N \\ \rho, & k = \alpha N + 1, \dots, N \end{cases} \quad (2.10)$$

Note that TS and SPS are two special cases of OPS by letting $\rho = 0$ (for TS) or $\alpha = 0$ (for SPS) in (2.10).

This thesis considers only the SPS and TS schemes. For convenience, we will use the term PS for the former scheme.

2.3 Energy harvesting and information decoding

In this section, the energy harvesting and information decoding procedures will be presented. To that end, the expressions of $y_{EH}(t)$ and $y_{ID}[k]$ (Figure 2.3) need first be derived. Taking into account (2.1), (2.2) and (2.5), the received signal (2.7) can be written as:

$$y(t) = \sqrt{2} \Re\{y_c(t)e^{j2\pi f_c t}\} \quad (2.11)$$

where $y_c(t)$ denotes the equivalent complex received signal, which is equal to:

$$y_c(t) = \sqrt{L} \sum_{i=1}^{n_T} h_i x_i(t) + n_A(t) = \sqrt{L} \sum_{i=1}^{n_T} |h_i| A_i(t) e^{j(\phi_i(t) + \theta_i)} + n_I(t) + j n_Q(t) \quad (2.12)$$

We write $y_c(t)$ in its polar form:

$$y_c(t) = A_y(t)e^{j\phi_y(t)} \quad (2.13)$$

where the amplitude $A_y(t)$ and the phase $\phi_y(t)$ are given by:

$$A_y(t) = \left| \sqrt{L} \sum_{i=1}^{n_T} h_i x_i(t) + n_A(t) \right| = \left| \sqrt{L} \mathbf{h}^H \mathbf{x}(t) + n_A(t) \right| \quad (2.14)$$

and

$$\phi_y(t) = \frac{n_Q(t) + \sqrt{L} \sum_{i=1}^{n_T} |h_i| A_i(t) \sin(\phi_i(t) + \theta_i)}{n_I(t) + \sqrt{L} \sum_{i=1}^{n_T} |h_i| A_i(t) \cos(\phi_i(t) + \theta_i)} \quad (2.15)$$

We should note that \mathbf{h} denotes the vector with complex entries $h_i^* = |h_i| e^{-j\theta_i}$, $i \in \{1, \dots, n_T\}$.

We also define h_{sum} as:

$$h_{sum} \triangleq |\mathbf{h}|^2 = \sum_{i=1}^{n_T} |h_i|^2 \quad (2.16)$$

By substituting (2.13) into (2.11), we re-express $y(t)$ as follows:

$$y(t) = A_y(t) \cos(2\pi f_c t + \phi(t)) \quad (2.17)$$

With an input voltage proportional to $y(t)$, the output current $i(t)$ of a Schottky diode is given by (Figure 2.2):

$$i(t) = I_s(e^{\gamma y(t)} - 1) = \sum_{n=1}^{\infty} a_n y^n(t) \quad (2.18)$$

where I_s denotes the saturation current, γ the reciprocal of the thermal voltage of the Schottky diode, and the n -th coefficient a_n is given by $a_n = I_s \gamma^n / n!$, due to the Taylor series expansion of the exponential function. By substituting (2.17) into (2.18) and ignoring the high-order (larger than two) terms of $y(t)$, we obtain:

$$i(t) \approx a_1 A_y(t) \cos(2\pi f_c t + \phi(t)) + \frac{1}{2} a_2 A_y^2(t) + \frac{1}{2} a_2 A_y^2(t) \cos(4\pi f_c t + 2\phi_y(t)) \quad (2.19)$$

The output current $i(t)$ of the diode is processed by a LPF, through which the high-frequency harmonic components at both f_c and $2f_c$ in $i(t)$ are removed and DC signal $i_{DC}(t)$ appears as the output of the rectifier. Assuming that the additive noise introduced by the rectifier is $n_{rec}(t)$, the filtered output $i_{DC}(t)$ is thus given by:

$$i_{DC}(t) = \frac{1}{2} a_2 A_y^2(t) + n_{rec}(t) \quad (2.20)$$

Since a_2 is a constant specified by the diode, for convenience we assume in sequel that $a_2 = 1$ (with $n_{rec}(t)$ normalized accordingly to maintain the signal-to-noise ratio (SNR)). We note that in (2.20) a_2 involves a unit conversion from a power signal to a current signal, thus by

normalization $n_{rec}(t)$ can equivalently be viewed as a power signal. Assume $n_{rec}(t) \sim \mathcal{N}(0, \sigma_{rec}^2)$, where σ_{rec} is in watt. Substituting (2.14) into (2.20) yields:

$$i_{DC}(t) = \left| \sqrt{L} \mathbf{h}^H \mathbf{x}(t) + n_A(t) \right|^2 + n_{rec}(t) \quad (2.21)$$

At this point, we assume that the converted power to be stored in the battery is linearly proportional to $i_{DC}(t)$, with a conversion efficiency $0 \leq \zeta \leq 1$ (the next chapter considers also a nonlinear energy harvesting model, without interfering with the analysis below, though). Hence, in the case where the received signal is used only for energy harvesting, the average power (normalized by the symbol period) stored in the battery, denoted by Q in watt or joule/sec, is given by $Q = \zeta P_r$ where $P_r = \mathbb{E}[i_{DC}(t)]$ denotes the average received power. Assuming that the antenna noise $n_A(t)$ is independent of $\mathbf{x}(t)$ and taking into account (2.4), (2.16) and the fact that $\mathbb{E}[n_{rec}(t)] = 0$, we compute the harvested energy:

$$\begin{aligned} Q &= \zeta \mathbb{E}[i_{DC}(t)] = \zeta \mathbb{E} \left[\left| \sqrt{L} \mathbf{h}^H \mathbf{x}(t) + n_A(t) \right|^2 \right] \\ &= \zeta \mathbb{E} \left[\left(\sqrt{L} \mathbf{h}^H \mathbf{x}(t) + n_A(t) \right) \left(\sqrt{L} \mathbf{h}^H \mathbf{x}(t) + n_A(t) \right)^H \right] \\ &= \zeta \mathbb{E} \left[\left(\sqrt{L} \mathbf{h}^H \mathbf{x}(t) + n_A(t) \right) \left(\sqrt{L} \mathbf{x}^H(t) \mathbf{h} + n_A^*(t) \right) \right] \\ &= \zeta \left(L \mathbf{h}^H \mathbb{E}[\mathbf{x}(t) \mathbf{x}^H(t)] \mathbf{h} + \mathbb{E}[|n_A(t)|^2] \right) \\ &= \zeta \left(L h_{sum} \hat{\mathbf{h}}^H \mathbf{S}_{xx} \hat{\mathbf{h}} + \sigma_A^2 \right) \end{aligned} \quad (2.22)$$

where $\hat{\mathbf{h}}$ denotes the normalized vector \mathbf{h} , i.e. $\hat{\mathbf{h}} = \mathbf{h}/|\mathbf{h}|$. Therefore, maximizing the harvested energy results in the following maximization problem:

$$\begin{aligned} \max_{\mathbf{S}_{xx}} \quad & q = \hat{\mathbf{h}}^H \mathbf{S}_{xx} \hat{\mathbf{h}} \\ \text{s.t.} \quad & \text{tr}(\mathbf{S}_{xx}) \leq P, \mathbf{S}_{xx} \succeq 0 \end{aligned}$$

Proposition 1. *The optimal solution to the above optimization problem is $\mathbf{S}_{xx}^{opt} = P \hat{\mathbf{h}} \hat{\mathbf{h}}^H$*

Proof. The proof of the proposition is based on [7]. Without loss of generality, we can write the optimal solution of the problem in its eigenvalue decomposition form as $\mathbf{S}_{xx}^{opt} = \mathbf{V} \mathbf{\Sigma} \mathbf{V}^H$, where $\mathbf{\Sigma} = \text{diag}(p_1, \dots, p_{n_T})$ and $\mathbf{V} = [\mathbf{v}_1, \dots, \mathbf{v}_{n_T}]$, where \mathbf{V} is an orthogonal matrix, which means that the vectors \mathbf{v}_i are normalized. Hence, the objective function and the condition of the problem can be written as:

$$q = \hat{\mathbf{h}}^H \mathbf{S}_{xx} \hat{\mathbf{h}} = \hat{\mathbf{h}}^H \mathbf{V} \mathbf{\Sigma} \mathbf{V}^H \hat{\mathbf{h}} = (\mathbf{V}^H \hat{\mathbf{h}})^H \mathbf{\Sigma} \mathbf{V}^H \hat{\mathbf{h}} = \sum_{i=1}^{n_T} p_i |\mathbf{v}_i^H \hat{\mathbf{h}}|^2 \quad (2.24)$$

where the last equation is valid, since the term $\mathbf{V}^H \hat{\mathbf{h}}$ is equal to

$$\mathbf{V}^H \hat{\mathbf{h}} = \begin{bmatrix} \mathbf{v}_1^H \\ \vdots \\ \mathbf{v}_{n_T}^H \end{bmatrix} \hat{\mathbf{h}} = \begin{bmatrix} \mathbf{v}_1^H \hat{\mathbf{h}} \\ \vdots \\ \mathbf{v}_{n_T}^H \hat{\mathbf{h}} \end{bmatrix}$$

and

$$\text{tr}(\mathbf{S}_{xx}) = \sum_{i=1}^{n_T} p_i \leq P \quad (2.25)$$

From (2.4), $\mathbf{S}_{xx}^{opt} \succeq 0$ implies that $p_i \geq 0$, $i \in \{1, \dots, n_T\}$. Making use of (2.24), (2.25) and the fact that the vectors $\mathbf{v}_i, \hat{\mathbf{h}}$ are normalized, i.e., $|\mathbf{v}_i^H \hat{\mathbf{h}}| \leq 1$, $\forall i \in \{1, \dots, n_T\}$, we can easily prove that the objective function is upper-bounded by P :

$$q = \sum_{i=1}^{n_T} p_i |\mathbf{v}_i^H \hat{\mathbf{h}}|^2 \leq \sum_{i=1}^{n_T} p_i \max_{\mathbf{v}_i} |\mathbf{v}_i^H \hat{\mathbf{h}}|^2 \leq P \quad (2.26)$$

In the last inequality, the equality holds if we choose $\sum_{i=1}^{n_T} p_i = P$ and $\mathbf{v}_i = \hat{\mathbf{h}}$, $\forall i \in \{1, \dots, n_T\}$. Hence, we obtain the optimal solution \mathbf{S}_{xx}^{opt} as:

$$\mathbf{S}_{xx}^{opt} = \mathbf{V} \Sigma \mathbf{V}^H = \sum_{i=1}^{n_T} p_i \mathbf{v}_i \mathbf{v}_i^H = \hat{\mathbf{h}} \hat{\mathbf{h}}^H \sum_{i=1}^{n_T} p_i = P \hat{\mathbf{h}} \hat{\mathbf{h}}^H \quad (2.27)$$

The proof of the Proposition 1 is thus completed. \square

Proposition 1 implies that \mathbf{S}_{xx}^{opt} is a rank-one matrix. Consequently, the maximum harvested power can be achieved by *beamforming* at the transmitter, which aligns with the vector $\hat{\mathbf{h}}$, i.e., the transmitted signal can be written as $\mathbf{x}(t) = \hat{\mathbf{h}}s(t)$, where $\mathbb{E}[s(t)] = 0$ and $\mathbb{E}[s^2(t)] = P$. The maximum harvested energy is derived by substituting (2.27) into (2.22):

$$Q = \zeta(Lh_{sum}P + \sigma_A^2) \quad (2.28)$$

As discussed in section 2.2, this thesis considers two SWIPT strategies, i.e., PS and TS. When the power-splitting protocol is used, the DC signal splits into two streams, one proportional to the PS factor $\rho \in [0, 1]$ for EH and one proportional to the factor $1 - \rho$ for ID (Figure 2.4). When the time-switching protocol is used, the DC signal is used for EH for the portion of time $\alpha \in [0, 1]$, whereas for the portion $1 - \alpha$ is used for ID (2.5).

Hence, in the case where the maximum average power P is exploited by the transmitter, i.e., $\mathbb{E}[s^2(t)] = P$, the maximum harvested energy for the PS and TS schemes is equal to [13]:

$$Q_{PS} = \rho \zeta(Lh_{sum}P + \sigma_A^2) \quad (2.29)$$

and

$$Q_{TS} = \alpha \zeta(Lh_{sum}P + \sigma_A^2) \quad (2.30)$$

As shown in Figure 2.3, a portion of the DC signal is processed by an analog-to-digital converter (ADC). Thus, the output of the noiseless power splitter and the ADC, y_{ID} , is derived by setting $\mathbf{x}(t) = \hat{\mathbf{h}}s(t)$ in (2.21):

$$y_{ID}[k] = (1 - \rho_k) \left(\left| \sqrt{L} |\mathbf{h}| s[k] + n_A[k] \right|^2 + n_{rec}[k] \right) + n_{ADC}[k] \quad (2.31)$$

where k denotes discrete time and $n_{ADC} \sim \mathcal{N}(0, \sigma_{ADC}^2)$ denotes the additive noise introduced by the ADC. Consequently, for PS and TS, (2.31) becomes:

$$y_{ID,PS}[k] = (1 - \rho) \left(\left| \sqrt{L} |\mathbf{h}| s[k] + n_A[k] \right|^2 + n_{rec}[k] \right) + n_{ADC}[k], \quad k = 1, \dots, N \quad (2.32)$$

and

$$y_{ID,TS}[k] = \begin{cases} 0, & k \leq \alpha \\ \left| \sqrt{L} |\mathbf{h}| s[k] + n_A[k] \right|^2 + n_{rec}[k] + n_{ADC}[k], & k > \alpha \end{cases} \quad (2.33)$$

In the sequel, two additional assumptions are made:

- $s^2(t) \leq A$, $A \geq P$: this assumption generalizes the analysis as the maximum transmitted power is also upper-bound by A .
- $\sigma_A^2 \ll \sigma_{rec}$: this is a practically valid assumption, which implies that the rectifier noise is dominant over the antenna noise, which can thus be ignored ($\sigma_A^2 \rightarrow 0$).

Based on (2.32), (2.33), and using the definition (2.16), the equivalent discrete-time memoryless channel for both PS and TS is modeled as:

$$Y = hX + Z, \quad \mathbb{E}[X] \leq P, \quad 0 \leq X \leq A, \quad Z \sim N(0, \sigma_z^2) \quad (2.34)$$

where

$$h = Lh_{sum} \quad (2.35)$$

while the variance of the equivalent processing noise for PS and TS respectively is given by:

$$\sigma_{z,PS}^2 = \sigma_{rec}^2 + \frac{\sigma_{ADC}^2}{(1-\rho)^2} \quad (2.36)$$

$$\sigma_{z,TS}^2 = \sigma_{rec}^2 + \sigma_{ADC}^2 \quad (2.37)$$

Note that the expression in (2.34) highlights the importance of the ADC noise, since it becomes evident from (2.36) that ignoring this renders the equivalent channel output, Y , independent to the PS factor. The channel (2.34) is known as the optical intensity channel, where X denotes the signal power, which is the non-negative channel input. The capacity of this channel is thoroughly analyzed in the next chapter.

The authors of [30] proved, using the symmetry of the channel law and the concavity of the mutual information in the input distribution, that, if the allowed average power is larger than half the allowed peak power, i.e., $A < 2P$, then the optimal input distribution of the optical intensity channel has mean value equal to $A/2$ [30, lemma 2]. By applying this lemma to (2.34), it follows that achieving the capacity of this channel entails the average transmit power (that is, the average power of the signal $s(t)$) is less than P if $A < 2P$ (in case where $A \geq 2P$ the average transmit power can be equal to P). However, the maximum harvested energy (2.28) thus decreases, as it is given by $Q' = \zeta(Lh_{sum}P' + \sigma_A^2)$, where $P' < P$. For the capacity of the channel to always be maximum, in this thesis we choose:

$$\mathbf{x}(t) = \hat{\mathbf{h}} s(t), \quad \mathbb{E}[s(t)] = 0, \quad \mathbb{E}[s^2(t)] = \mathcal{E}, \quad s^2(t) \leq A \quad (2.38)$$

where \mathcal{E} is defined as:

$$\mathcal{E} \triangleq \begin{cases} P, & A \geq 2P \\ A/2, & A < 2P \end{cases} \quad (2.39)$$

Consequently, taking into account the assumption $\sigma_A^2 \rightarrow 0$ as well as the choice (2.38), the harvested energy for the PS and TS schemes is given by (2.29) and (2.30), respectively, where $P = \mathcal{E}$.

2.4 Fading channel and path loss factor modeling

According to the analysis of the previous section, the equivalent communication channel is given by (2.35). This section aims at modeling the two terms in (2.35), namely L and h_{sum} .

The path loss factor can be accurately approximated as [31]:

$$L = 1 - e^{-\beta} \quad (2.40)$$

where β is given by

$$\beta = \frac{a_T a_R}{(\lambda d)^2} \quad (2.41)$$

Note that Eq. (2.41) is equivalent to the Friis equation for far-field transmission, where a_T , a_R denote the apertures of the transmit and receive arrays respectively, λ denotes the wavelength in vacuum, and d denotes the propagation distance. The propagation as described in (2.40) covers both the near and far fields. For the far field where β is small (large d), the propagation path loss factor is approximately equal to β , thus following the Friis transmission equation. For the near field where d is small and hence β is large, the path loss factor is close to one.

We assume that the random variables h_i all are independent and $h_i \sim \mathcal{CN}(0, \sigma_h^2)$, $\forall i \in \{1, \dots, n_T\}$. Consequently $|h_i|$ follows a Rayleigh distribution with scale parameter $\sigma_h^2 \sqrt{2}/2$, i.e., $|h_i| \sim \text{Rayleigh}(\sigma_h^2 \sqrt{2}/2)$, whereas $|h_i|^2$ follows an exponential distribution with rate parameter $1/\sigma_h^2$, i.e., $|h_i|^2 \sim \exp(1/\sigma_h^2)$. Nevertheless, the exponential distribution constitutes a special case of the Gamma distribution, denoted as $\text{Gamma}(k, \theta)$, where k , θ denote the shape parameter and the scale parameter, respectively. The corresponding probability density function in the shape-rate parametrization is

$$f(x; k, \theta) = \frac{x^{k-1} e^{-\frac{x}{\theta}}}{\theta^k \Gamma(k)}, \quad x > 0 \text{ and } k, \theta > 0 \quad (2.42)$$

whereas the cumulative distribution function is the regularized gamma function

$$F(x; k, \theta) = \int_0^x f(t; k, \theta) dt = \frac{\gamma(k, \frac{x}{\theta})}{\Gamma(k)} \quad (2.43)$$

where $\Gamma(x)$, $\gamma(s, x)$ are the gamma function and the lower incomplete gamma function, respectively, which are defined as:

$$\Gamma(x) = \int_0^\infty t^{x-1} e^{-t} dt, \quad x > 0 \quad (2.44)$$

$$\gamma(s, x) = \int_0^x t^{s-1} e^{-t} dt, \quad x > 0 \quad (2.45)$$

An important property of the gamma function is the following:

$$\Gamma(n) = (n-1)!, \quad n \in \mathbb{Z}_+ \quad (2.46)$$

Based on (2.42), we can write $|h_i|^2 \sim \text{Gamma}(1, \sigma_h^2)$, $\forall i \in \{1, \dots, n_T\}$. Hence, the random variable h_{sum} defined in (2.16) is the sum of n_T independent random variables, all following a gamma distribution with the same scale parameter σ_h^2 . This results in [32]:

$$h_{sum} \sim \text{Gamma}(n_T, \sigma_h^2) \quad (2.47)$$

That is, h_{sum} follows a gamma distribution where the shape parameter is equal to the sum of the shape parameters of the RVs $|h_i|^2$ ($k = n_T \in \mathbb{Z}_+$), and the rate parameter is identical to their common rate parameter ($\theta = \sigma_h^2$). Taking in to account (2.43), (2.46) and (2.47), we compute the probability:

$$\Pr(h_{sum} \leq x) = \frac{1}{(n_T - 1)!} \gamma\left(n_T, \frac{x}{\sigma_h^2}\right) \quad (2.48)$$

The result in (2.48) will be used in the next chapter.

Chapter 3

System performance evaluation

This chapter aims at presenting the two fundamental performance metrics of the SWIPT systems, namely the *rate-energy region* and the *joint rate-energy outage probability*, which quantify the tradeoff between energy and information transmission. To that end, the first section studies the capacity of the optical intensity channel with peak and average power constraints, which determines the information rate of the system, whereas the second section analyzes two widely used energy harvesting models that determine the energy stored in the battery. Subsequently, in the last section the achievable rate-energy region is presented and the optimal operating point in this region is specified by minimizing the outage probability, taking into consideration both EH models.

3.1 Optical intensity channel with peak and average power constraints

As discussed in the previous chapter, the equivalent discrete-time memoryless channel is known as the optical intensity channel with peak and average power constraint. A mathematical representation for this channel is given by:

$$Y = hX + Z, \quad h \geq 0, \quad \mathbb{E}[X] \leq P, \quad 0 \leq X \leq A, \quad Z \sim \mathcal{N}(0, \sigma_z^2) \quad (3.1)$$

For the sake of brevity, we use the terms APC and PPC to refer to the Average Power Constraint and Peak Power Constraint, respectively. We also define the ratio between the allowed peak power and the allowed average power by r :

$$r \triangleq \frac{PPC}{APC} = \frac{A}{P} \geq 1 \quad (3.2)$$

Note that for $r = 1$ the APC is inactive in the sense that it has no influence on the capacity and is automatically satisfied whenever the PPC is satisfied. Thus, $r = 1$ corresponds to the case with only a PPC. Similarly, $r \gg 1$ corresponds to a dominant APC and only a weak PPC.

It should be mentioned that in (3.1) we assume that the random variable Z follows a normal distribution with zero mean value and variance equal to σ_z^2 (σ_z is in watt). Hence, the probability density function of Z is given by:

$$f_z(z) = \frac{1}{\sqrt{2\pi\sigma_z^2}} e^{-\frac{z^2}{2\sigma_z^2}} \quad (3.3)$$

while its entropy can be easily obtained [33]:

$$H(Z) = \frac{1}{2} \log_2(2\pi e \sigma_z^2) \quad (3.4)$$

The optical signal-to-noise ratio (SNR) for a given channel realization h is defined as [34]:

$$\text{SNR}(h) = \frac{hP}{\sigma_z} \quad (3.5)$$

3.1.1 Bounds on channel capacity

A lower bound on the capacity of the channel can be derived using the Entropy Power Inequality (EPI). The channel capacity relates to the mutual information between the input and the output of the channel through the inequality

$$C \geq I(X; Y) \quad (3.6)$$

where the equality holds for the optimal input distribution. From (3.6), a capacity lower bound can be obtained using a random input distribution subject to the APC and PPC constraints. The mutual information between the input and the output of the channel (3.1) can be written as:

$$I(X; Y) = H(Y) - H(Y|X) = H(hX + Z) - H(Z) = \frac{1}{2} \log_2(2^{2H(hX+Z)}) - \frac{1}{2} \log_2(2^{2H(Z)}) \quad (3.7)$$

For the first term in (3.7), the EPI yields [33]:

$$\frac{1}{2} \log_2(2^{2H(hX+Z)}) \geq \frac{1}{2} \log_2(2^{2H(hX)} + 2^{2H(Z)}) \quad (3.8)$$

As a result of (3.7) and (3.8), the mutual information is lower-bounded by:

$$I(X; Y) \geq \frac{1}{2} \log_2(2^{2H(hX)} + 2^{2H(Z)}) - \frac{1}{2} \log_2(2^{2H(Z)}) \quad (3.9)$$

Substituting (3.4) into (3.9) and then (3.9) into (3.6), and taking into consideration that $H(hX) = H(X) + \log_2(h)$, we have:

$$C \geq \frac{1}{2} \log_2 \left(1 + \frac{2^{2(H(X)+\log_2(h))}}{2\pi e \sigma_z^2} \right) \quad (3.10)$$

From (3.10) we deduce that getting a tight lower bound on capacity is equivalent to maximizing the differential entropy of X subject to the APC and PPC constraints. The solution to this maximization problem is given by [30]:

$$f_x^{lb}(x) = \begin{cases} \frac{1}{A}, & r \leq 2 \\ \frac{1}{A} \frac{\mu^*}{1 - e^{-\mu^*}} e^{-\frac{\mu^* x}{A}}, & r > 2 \end{cases} \quad 0 \leq x \leq A \quad (3.11)$$

where μ^* is chosen such us the APC is satisfied, i.e., μ^* is given as the (unique for a specified value of r) solution to

$$\frac{1}{r} = \frac{1}{\mu^*} + \frac{1}{1 - e^{-\mu^*}} \quad (3.12)$$

We observe that the mean value of the random variable X with probability density function $f_x^{lb}(x)$ given in (3.11) is equal to $A/2$ when $r \leq 2$, or P when $r > 2$. Therefore $\mathbb{E}[X] = \mathcal{E}$, where \mathcal{E} is defined in (2.39). For both cases $r \leq 2$ and $r > 2$, we derive a tight lower bound on capacity, denoted as R_{lb} , by computing the differential entropy of X and substituting the result in (3.10).

- $r \leq 2$:

$$H(X) = \log_2(A) \quad (3.13)$$

Substituting (3.13) into (3.10) we obtain:

$$R_{lb} = \frac{1}{2} \log_2 \left(1 + \frac{2^{2(\log_2(A) + \log_2(h))}}{2\pi e \sigma_z^2} \right) = \frac{1}{2} \log_2 \left(1 + \frac{(hA)^2}{2\pi e \sigma_z^2} \right) = \frac{1}{2} \log_2 \left(1 + \frac{(rhP)^2}{2\pi e \sigma_z^2} \right) \quad (3.14)$$

- $r > 2$:

$$\begin{aligned} H_e(X) &= - \int_0^A f_x^{lb}(x) \log(f_x^{lb}(x)) dx = - \int_0^A \frac{1}{A} \frac{\mu^*}{1 - e^{-\mu^*}} e^{-\frac{\mu^* x}{A}} \log \left(\frac{1}{A} \frac{\mu^*}{1 - e^{-\mu^*}} e^{-\frac{\mu^* x}{A}} \right) dx \\ &= - \log \left(\frac{1}{A} \frac{\mu^*}{1 - e^{-\mu^*}} \right) \int_0^A \frac{1}{A} \frac{\mu^*}{1 - e^{-\mu^*}} e^{-\frac{\mu^* x}{A}} dx + \frac{\mu^*}{A} \int_0^A \frac{x}{A} \frac{\mu^*}{1 - e^{-\mu^*}} e^{-\frac{\mu^* x}{A}} dx \\ &= - \log \left(\frac{1}{A} \frac{\mu^*}{1 - e^{-\mu^*}} \right) \int_0^A f_x^{lb}(x) dx + \frac{\mu^*}{A} \int_0^A x f_x^{lb}(x) dx \\ &= \frac{\mu^*}{r} - \log \left(\frac{1}{A} \frac{\mu^*}{1 - e^{-\mu^*}} \right) = \frac{\mu^*}{r} - \frac{\log_2 \left(\frac{1}{A} \frac{\mu^*}{1 - e^{-\mu^*}} \right)}{\log_2(e)} \end{aligned}$$

since $\int_0^A f_x^{lb}(x) dx = 1$ and $\frac{1}{A} \int_0^A x f_x^{lb}(x) dx = \frac{1}{A} \mathbb{E}[X] = \frac{P}{A} = \frac{1}{r}$. Hence:

$$H(X) = \log_2(e) H_e(X) = \frac{\mu^*}{r} \log_2(e) - \log_2 \left(\frac{1}{A} \frac{\mu^*}{1 - e^{-\mu^*}} \right) \quad (3.15)$$

In order for the capacity lower bound to be derived, in this case we use (3.15) to initially compute the quantity:

$$2^{2(H(X) + \log_2(h))} = h^2 2^{2\frac{\mu^*}{r} \log_2(e)} 2^{-2 \log_2 \left(\frac{1}{A} \frac{\mu^*}{1 - e^{-\mu^*}} \right)} = \frac{h^2 e^{\frac{2\mu^*}{r}}}{\left(\frac{1}{A} \frac{\mu^*}{1 - e^{-\mu^*}} \right)^2} = \frac{(rhP)^2 e^{\frac{2\mu^*}{r}}}{\left(\frac{\mu^*}{1 - e^{-\mu^*}} \right)^2}$$

Substituting the above result into (3.10), the capacity lower bound is written as:

$$R_{lb} = \frac{1}{2} \log_2 \left(1 + \frac{(rhP)^2 e^{\frac{2\mu^*}{r}}}{2\pi e \sigma_z^2 \left(\frac{\mu^*}{1 - e^{-\mu^*}} \right)^2} \right) = \frac{1}{2} \log_2 \left(1 + \frac{(rhP)^2}{2\pi e \sigma_z^2} \left(\frac{1 - e^{-\mu^*}}{\mu^* e^{-\frac{\mu^*}{r}}} \right)^2 \right) \quad (3.16)$$

Making use of (3.5) and defining the function $v(r)$ as in (3.18), the capacity lower bound can be expressed as:

$$R_{lb} = \frac{1}{2} \log_2 \left(1 + \frac{(v(r) \text{SNR}(h))^2}{2\pi e} \right) \quad (3.17)$$

where

$$v(r) = \begin{cases} r, & 1 \leq r \leq 2 \\ \frac{r(1 - e^{-\mu^*})}{\mu^* e^{-\frac{\mu^*}{r}}}, & r > 2 \end{cases} \quad (3.18)$$

where μ^* is given as the (unique for a specified value of r) solution to (3.12). To sum up, the input distribution (3.11) achieves the capacity lower bound (3.17) and has mean value equal to \mathcal{E} , that is $\mathbb{E}[X] = \mathcal{E}$. We should also note that this lower bound is in [bits/channel use]. If we change the base of the logarithm from 2 into e , then the lower bound is in [nats/channel use] [30].

In the sequel, we will study the function $v(r)$. To that end, the equation (3.12) has to be further explored. For convenience, it is rewritten as:

$$g(\mu^*) = \frac{1}{r} \quad (3.19)$$

where the function g is defined as:

$$g(x) = \frac{1}{x} + \frac{1}{1 - e^x}, \quad x \in \mathbb{R}^* \quad (3.20)$$

At first, two lemmas regarding this function will be proved.

Lemma 1. *The function $g(x)$ is strictly decreasing for $x \in \mathbb{R}^*$.*

Proof. Firstly, we should note that to determine the monotonicity of g is not an obvious task, since g is the sum of a decreasing and an increasing function. We thus take the first derivative of $g(x)$:

$$g'(x) = -\frac{1}{x^2} + \frac{e^x}{(1 - e^x)^2} = \frac{-e^{2x} - 1 + (x^2 + 2)e^x}{x^2(1 - e^x)^2} = \frac{e^x(x^2 + 2 - e^{-x} - e^x)}{x^2(1 - e^x)^2}$$

At this point, we define the function $A(x)$ as:

$$A(x) = x^2 + 2 - e^{-x} - e^x = x^2 + 2 - 2 \cosh(x), \quad x \in \mathbb{R}$$

The first derivative of g can thus be rewritten as:

$$g'(x) = \frac{e^x A(x)}{x^2(1 - e^x)^2}$$

We observe that the sign of $A(x)$ determines the sign of $g'(x)$, since the functions e^x , x^2 and $(1 - e^x)^2$ are all non-negative. Taking the first two derivatives of $A(x)$, we obtain:

$$A'(x) = 2x - 2 \sinh(x), \quad A'(0) = 0$$

$$A''(x) = 2 - 2 \cosh(x), \quad A''(0) = 0$$

Since $\cosh(x) \geq 1$ where equality holds for $x = 0$, we deduce that $A''(x) \leq 0$, which yields $A'(x) \downarrow$. Hence it holds that:

$$x \leq 0 \Rightarrow A'(x) \geq A'(0) = 0 \quad \text{and} \quad x \geq 0 \Rightarrow A'(x) \leq A'(0) = 0$$

That is, $A(x)$ attains at $x = 0$ its maximum value $A(0) = 0$. Consequently $A(x) < 0, \forall x \in \mathbb{R}^*$, whereupon $g'(x) < 0, \forall x \in \mathbb{R}^*$ resulting in $g \downarrow$, which completes the proof. \square

Lemma 2. *The following limits are valid: $\lim_{x \rightarrow \infty} g(x) = 0, \lim_{x \rightarrow -\infty} g(x) = 1, \lim_{x \rightarrow 0} g(x) = \frac{1}{2}$*

Proof. Since the first two limits are quite obvious, we will prove only the third limit applying the L'Hospital's Rule:

$$\lim_{x \rightarrow 0} g(x) = \lim_{x \rightarrow 0} \left(\frac{1}{x} + \frac{1}{1 - e^x} \right) = \lim_{x \rightarrow 0} \frac{x + 1 - e^x}{x - xe^x} = \lim_{x \rightarrow 0} \frac{1 - e^x}{1 - e^x - xe^x} = \lim_{x \rightarrow 0} \frac{-e^x}{-2e^x - xe^x} = \frac{1}{2}$$

□

Due to Lemma 1, g is a monotonous functions and thus a one-to-one function, which implies that the equation (3.19) has a unique solution μ^* for a specified value of r . Due to Lemma 2 and taking into consideration that $r \geq 1$, it holds that $(\mu^* \rightarrow +\infty \Rightarrow r \rightarrow +\infty)$ and $(\mu^* \rightarrow 0 \Rightarrow r \rightarrow 2)$, which can become more strict since g is a one-to-one function: $(\mu^* \rightarrow +\infty \Leftrightarrow r \rightarrow +\infty)$ and $(\mu^* \rightarrow 0 \Leftrightarrow r \rightarrow 2)$. These conclusions lead to the following proposition:

Proposition 2. *The function $v(r)$ is continuous at $r = 2$, and its codomain is $[1, e)$.*

Proof. Since $r \geq 1$, we have to prove that:

$$\lim_{r \rightarrow 2^+} v(r) = 2, \quad \lim_{r \rightarrow +\infty} v(r) = e$$

Both limits regard the case where $r > 2$. In this case, v is given by (3.18) and thus can be rewritten as:

$$v(x) = \frac{1 - e^{-x}}{y(x)e^{-y(x)}}$$

where $x = \mu^*$, whereas $y(x)$ is derived by setting $x = \mu^*$ in (3.12): $y = \frac{\mu^*}{r} = 1 + \frac{\mu^*}{1 - e^{\mu^*}} \Rightarrow y(x) = 1 + \frac{x}{1 - e^x}$. Hence, the limits can be expressed as:

$$\lim_{x \rightarrow 0^+} v(x) = 2, \quad \lim_{x \rightarrow +\infty} v(x) = e$$

due to $(\mu^* \rightarrow 0^+ \Leftrightarrow r \rightarrow 2^+)$ and $(\mu^* \rightarrow +\infty \Leftrightarrow r \rightarrow +\infty)$, respectively. To evaluate these limits, we need to evaluate the following limits using the L'Hospital's rule.

$$\lim_{x \rightarrow +\infty} y(x) = 1 + \lim_{x \rightarrow +\infty} \frac{x}{1 - e^x} = 1$$

$$\lim_{x \rightarrow 0^+} y(x) = \lim_{x \rightarrow 0^+} \left(1 + \frac{x}{1 - e^x} \right) = \lim_{x \rightarrow 0^+} \frac{x + 1 - e^x}{1 - e^x} = \lim_{x \rightarrow 0^+} \frac{1 - e^x}{-e^x} = 0$$

Hence:

$$\lim_{x \rightarrow +\infty} v(x) = \lim_{x \rightarrow +\infty} \frac{1 - e^{-x}}{y(x)e^{-y(x)}} = \frac{\lim_{x \rightarrow +\infty} (1 - e^{-x})}{\lim_{x \rightarrow +\infty} (y(x)e^{-y(x)})} = \frac{1}{1 \cdot e^{-1}} = e$$

and

$$\lim_{x \rightarrow 0^+} v(x) = \lim_{x \rightarrow 0^+} \frac{1 - e^{-x}}{y(x)e^{-y(x)}}$$

This limit involves indeterminate form $0/0$. The first derivative of $y(x)$ is $y'(x) = \frac{1 + (x - 1)e^x}{(1 - e^x)^2}$

and thus $\lim_{x \rightarrow 0^+} y'(x) = \lim_{x \rightarrow 0^+} \frac{x}{-2(1 - e^x)} = \lim_{x \rightarrow 0^+} \frac{1}{2e^x} = \frac{1}{2}$. Applying L'Hospital's rule, we have:

$$\lim_{x \rightarrow 0^+} v(x) = \lim_{x \rightarrow 0^+} \frac{e^{-x}}{(1 - y(x)) y'(x) e^{-y(x)}} = \frac{\lim_{x \rightarrow 0^+} e^{-x}}{\left(1 - \lim_{x \rightarrow 0^+} y(x) \right) e^{-\lim_{x \rightarrow 0^+} y(x)} \lim_{x \rightarrow 0^+} y'(x)} = 2$$

which completes the proof. □

Figure (3.1) illustrates the graph of the function $v(r)$ and confirms the Proposition 2. From (3.17) it is obvious that the capacity lower bound is an increasing function of v . Therefore, the graph shows that R_{lb} increases as the ratio r ranges from 1 to 6, whereas R_{lb} remains stable at e as $r \rightarrow +\infty$. Consequently, the case where $r \geq 6$ yields a dominant APC constraint over the PPC constraint.

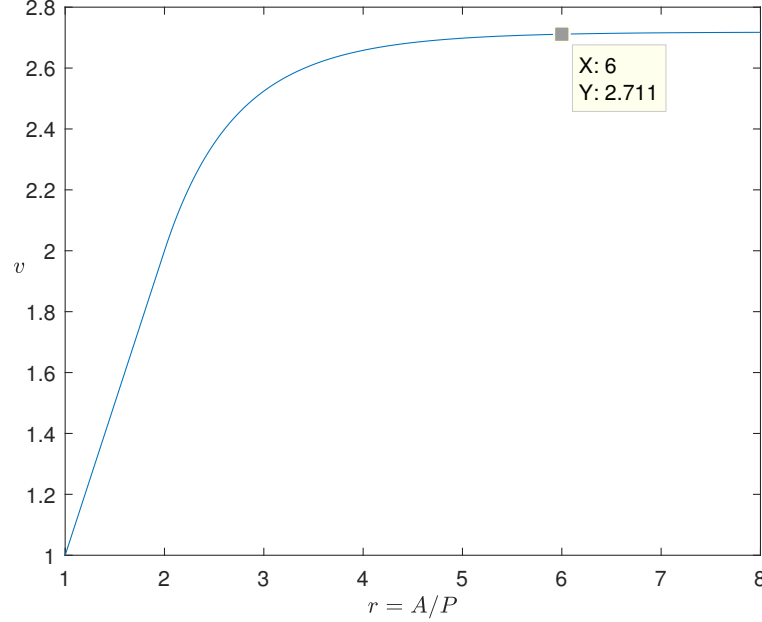


Figure 3.1: The graph of the function $v(r)$

Upper bounds on capacity for both cases, i.e., $r \leq 2$ and $r > 2$ have been derived in [30]. After some manipulation, we present the results in terms of r and SNR , which we denote as R_{ub} , without presenting the corresponding probability density functions that achieve these upper bounds, since they are complicated.

- $r \leq 2$

$$R_{ub} = \left(1 - 2\mathcal{Q}\left(s + \frac{\gamma}{2}\right)\right) \log\left(\frac{\gamma + 2s}{\sqrt{2\pi}(1 - 2\mathcal{Q}(s))}\right) - \frac{1}{2} + \mathcal{Q}(s) + \frac{s}{\sqrt{2\pi}}e^{-\frac{s^2}{2}} \quad (3.21)$$

- $r > 2$

$$\begin{aligned} R_{ub} = & \left(1 - \mathcal{Q}\left(s + \frac{\gamma}{r}\right) - \mathcal{Q}\left(s + \left(1 - \frac{1}{r}\right)\gamma\right)\right) \log\left(\gamma \frac{e^{\frac{\mu s}{\gamma}} - e^{-\mu\left(1 + \frac{s}{\gamma}\right)}}{\mu\sqrt{2\pi}(1 - 2\mathcal{Q}(s))}\right) - \frac{1}{2} \\ & + \mathcal{Q}(s) + \frac{s}{\sqrt{2\pi}}e^{-\frac{s^2}{2}} + \frac{\mu}{\gamma\sqrt{2\pi}}\left(e^{-\frac{s^2}{2}} - e^{-\frac{(\gamma+s)^2}{2}}\right) + \frac{\mu}{r}\left(1 - 2\mathcal{Q}\left(s + \frac{\gamma}{2}\right)\right) \end{aligned} \quad (3.22)$$

where $\mathcal{Q}(\cdot)$ denotes the \mathcal{Q} -function, $\gamma = r \text{SNR}(h)$, $s = \log(1 + \gamma)$ and $\mu = \mu^*\left(1 - e^{-\frac{s^2}{2r}}\right)$ with μ^* given by (3.12). In both (3.21) and (3.22), R_{ub} is in [nats/channel use]. We will use (3.21), (3.22) to confirm that the mutual information that approximates the capacity of the

optical intensity channel (which is described in the next subsection) does not exceed these upper bounds.

Figure 3.2 depicts the upper and lower bounds on capacity (in [nats/channel use]) for $r = 2$ and $r = 6$. Considering both graphs, we observe that an increase in r results in an upward shift of both bounds, whereas an increase in SNR decreases the gap between the upper and lower bounds. Hence in the high-SNR scenario, the lower bound approaches perfectly the capacity since the gap between them is negligible. Nevertheless, this is not the case for the low-SNR scenario, as the mutual information computed using a continuous input probability density function cannot approach the capacity. The next subsection thus addresses the case where the high-SNR does not apply to the optical intensity channel.

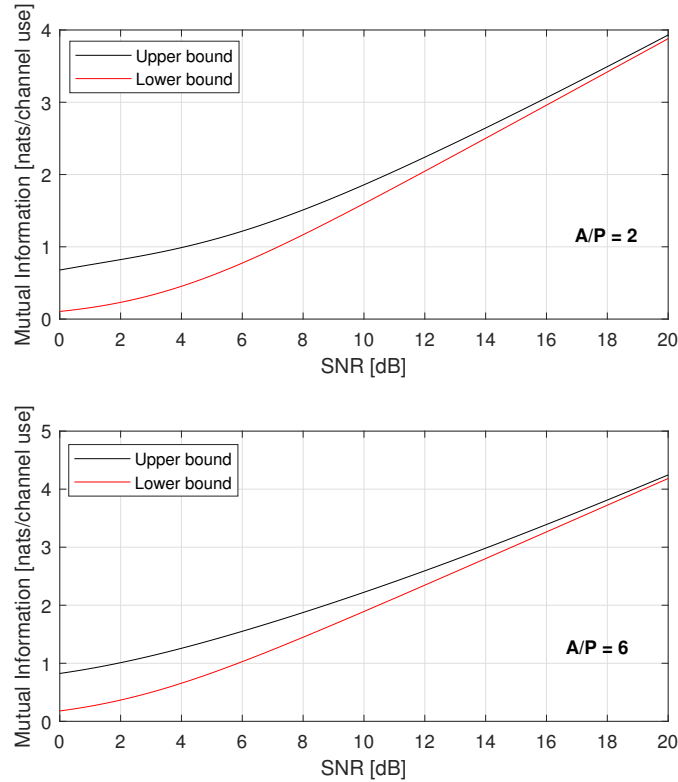


Figure 3.2: Upper and lower bounds on capacity for $r = 2$ and $r = 6$

3.1.2 Channel capacity approximation

The instantaneous channel capacity, $C(h)$, of (3.1), for a given channel state h is the maximum mutual information over the set \mathbb{F} and is given by:

$$C(h) = \max_{f_x(x) \in \mathbb{F}} I(X; Y|h) \quad (3.23)$$

where the *capacity-achieving* distribution is

$$f_x^*(x) = \arg \max_{f_x(x) \in \mathbb{F}} I(X; Y|h) \quad (3.24)$$

In general, $f_x^*(x)$ is different for each r and $\text{SNR}(h)$. For channels with constrained input amplitude and power, it was first shown in [35] that the capacity-achieving distribution is discrete

with a finite number of probability mass points, i.e., it can be expressed as:

$$f_x^*(x) = \sum_{k=0}^K a_k \delta(x - x_k) \quad (3.25)$$

where $f_x^*(x)$ should satisfy the APC and PPC constraints, as well as the properties of a probability density function:

$$a_k \geq 0, \quad \sum_{k=0}^K a_k = 1, \quad x_k \in [0, A], \quad \sum_{k=0}^K x_k a_k \leq P, \quad K \in \mathbb{Z}_+ \quad (3.26)$$

where the free parameters are a_k , x_k and K . For a given A , P , h and σ_z^2 , numerical optimization methods can be used to efficiently solve this non-linear optimization problem in (3.23) to find $f_x^*(x)$. However, finding an analytical closed form expression for the optimum distribution is difficult.

The high complexity of this optimization problem motivated the authors of [36] to develop a family of discrete non-uniform input distributions via entropy maximization. The developed distributions are termed *capacity-approaching* since it is numerically verified that, for different values of the peak-to-average ratio (r), they have rates close to the channel capacity over a wide range of signal-to-noise ration (SNRs). They also require fewer amplitude mass points, thereby making implementation simpler. Their simpler structure is exploited to develop a practical signalling algorithm in the rest of the paper.

In particular, it is assumed that the developed distributions $f_x^{ca}(x)$ have $K+1$ equally spaced mass points x_k in $[0, A]$, where the constant space between them is denoted as l :

$$f_x^{ca}(x) = \sum_{k=0}^K p_k \delta(x - kl), \quad l = \frac{A}{K} \quad (3.27)$$

The problem of maximizing the entropy of $f_x^{ca}(x)$ is solved in the sequel:

$$\max_{p_k} \sum_{k=0}^K p_k \log_2 \frac{1}{p_k} \quad (3.28)$$

where $p_k \geq 0$, $K \in \mathbb{Z}_+$, while the conditions (3.26) are rewritten for the input distribution $f_x^{ca}(x)$:

$$s.t. \quad \sum_{k=0}^K p_k = 1, \quad \sum_{k=0}^K kl p_k \leq P, \quad A = lK \quad (3.29)$$

The solution to the optimization problem (3.28)-(3.29) is:

- $r \leq 2$: p_k are uniformly distributed

$$p_k = \frac{1}{M} = \frac{1}{K+1}, \quad \mathbb{E}[X] = \frac{A}{2} \quad (3.30)$$

- $r > 2$: p_k are exponentially distributed

$$p_k = \frac{t_0^k}{\sum_{k=0}^K t_0^k}, \quad \mathbb{E}[X] = P \quad (3.31)$$

where $t_0 \in (0, 1]$ is the unique positive real root of

$$S(t) = \sum_{k=0}^K \left(1 - \frac{k}{K}r\right) t^k$$

The number of mass points that yields acceptable performance, that is, the resulting mutual information remains close to the channel capacity, is given by:

$$K + 1 = \left\lfloor \frac{r}{2.5} \text{SNR}(h) \right\rfloor \quad (3.32)$$

Based on the results (3.30) and (3.31), the mean value of the capacity-approaching distribution $f_x^{ca}(x)$ is

$$\mathbb{E}[X] = \mathcal{E}, \quad r \geq 1 \quad (3.33)$$

where \mathcal{E} is defined in (2.39). Note that this is also the case for the input distribution $f_x^{lb}(x)$ that achieves the capacity lower bound.

The rest of this subsection aims at deriving the expression of the mutual information that approaches the capacity, as this step is omitted in [36]. The mutual information between the input and the output of (3.1) can be written as:

$$I(X; Y) = H(Y) - H(Y|X) = H(Y) - H(Z) \quad (3.34)$$

To compute the output entropy, $H(Y)$, we initially have to derive the expression of the probability density function (PDF) of Y . To that end, we re-express the channel in (3.1) as:

$$Y = \bar{X} + Z \quad (3.35)$$

where $\bar{X} = hX$. It is known that for two random variables X, Y with PDFs $f_x(x), f_y(y)$, respectively, which are related to each other by the expression $Y = aX$, it holds that $f_y(y) = \frac{1}{|a|} f_x\left(\frac{y}{a}\right)$. Consequently, the PDF of \bar{X} is given by:

$$f_{\bar{x}}(\bar{x}) = \frac{1}{h} f_x\left(\frac{\bar{x}}{h}\right) = \sum_{k=0}^K p_k \frac{1}{h} \delta\left(\frac{\bar{x}}{h} - kl\right) = \sum_{k=0}^K p_k \delta(\bar{x} - klh) \quad (3.36)$$

where the last equation holds due to $|a|\delta(ax) = \delta(x)$, which constitutes a basic property of the δ -function. The term klh can equivalently be written as $klh = k\frac{A}{K}h = \frac{k}{K}rhP$. Additionally $X \perp Z$, which entails $\bar{X} \perp Z$. From (3.35) we can thus infer that Y is the sum of two independent random variables and consequently its PDF is given by the convolution of the PDFs of \bar{X} and Z , which are given by (3.36) and (3.3), respectively:

$$f_y(y) = f_{\bar{x}}(y) * f_z(y) = \left(\sum_{k=0}^K p_k \delta(y - klh) \right) * f_z(y) = \sum_{k=0}^K p_k f_z\left(y - \frac{k}{K}rhP\right) \quad (3.37)$$

Hence, the entropy of Y is

$$H(Y) = - \int_S f_y(y) \log_2(f_y(y)) dy = - \int_S g(y) dy \quad (3.38)$$

where $S = \mathbb{R}$ is the support set of Y and $g(y) = f_y(y) \log_2(f_y(y))$. Note that $g(y) \leq 0$, since $0 \leq f_y(y) \leq 1$.

From (3.37) it is obvious that $f_y(y)$ is identical to the sum of $K + 1$ gaussian functions, each being shifted by $\frac{k}{K}rhP$ and having an equal or exponentially decreasing amplitude p_k . This observation enables the integration of $g(y)$ over $S' \subset S$, i.e., over a subset of S , while the error remains small. It can be easily proved that $f_y(y) \rightarrow 0$ yields $g(y) \rightarrow 0$, and therefore $H(Y) \rightarrow 0$. Therefore $S' = S - \{y : f_y(y) < \epsilon\}$, where ϵ is a very small positive constant. To determine the subset S' , we recur to the following integrals regarding the gaussian function $G(x) = e^{-\frac{x^2}{2\sigma^2}}$:

$$\begin{aligned} \int_{-\infty}^{\infty} G(x) dx &= \int_{-\infty}^{\infty} e^{-\frac{x^2}{2\sigma^2}} dx = \sigma\sqrt{2\pi} \\ \int_{-\tau}^{\tau} G(x) dx &= \int_{-\tau}^{\tau} e^{-\frac{x^2}{2\sigma^2}} dx = \sigma\sqrt{2} \int_{-\frac{\tau}{\sigma\sqrt{2}}}^{\frac{\tau}{\sigma\sqrt{2}}} e^{-t^2} dt = 2\sqrt{2}\sigma \int_0^{\frac{\tau}{\sigma\sqrt{2}}} e^{-t^2} dt = \sigma\sqrt{2\pi} \operatorname{erf}\left(\frac{\tau}{\sigma\sqrt{2}}\right) \end{aligned}$$

where $\operatorname{erf}(\cdot)$ denotes the *error function*. By dividing the above integrals, we can derive the normalized integral of a gaussian function over the interval $\Delta_\tau = [-\tau, \tau]$:

$$\frac{\int_{-\tau}^{\tau} G(x) dx}{\int_{-\infty}^{\infty} G(x) dx} = \operatorname{erf}\left(\frac{\tau}{\sigma\sqrt{2}}\right)$$

Setting $\tau = 4\sigma$ in the above expression we obtain $\operatorname{erf}(2\sqrt{2}) = 0.999$, that is, the area of $G(x)$ on $\Delta_T = [-4\sigma, 4\sigma]$ is almost equal to the area of $G(x)$ on \mathbb{R} .

Let $S' = [l_d, l_u]$ and $\Delta_T^k = [l_d^k, l_u^k]$ be the Δ_T -interval of the k -th gaussian function in (3.37), Based on the previous analysis, we choose:

- $l_d = l_d^0 = 0 - 4\sigma_z = -4\sigma_z$
- $l_u = l_u^K = Klh + 4\sigma_z = K\frac{A}{K}h + 4\sigma_z = 4\sigma_z + rhP$

Therefore, the integral in (3.38) can be perfectly approximated as:

$$H(Y) \approx - \int_{S'} g(y) dy = - \int_{l_d}^{l_u} g(y) dy = - \int_{-4\sigma_z}^{4\sigma_z + rhP} f_y(y) \log_2(f_y(y)) dy \quad (3.39)$$

Substituting (3.39) and (3.4) into (3.34), we derive the mutual information that approaches the channel capacity, which we denote as R_{ca} :

$$R_{ca} = - \int_{-4\sigma_z}^{4\sigma_z + rhP} f_y(y) \log_2(f_y(y)) dy - \frac{1}{2} \log_2(2\pi e\sigma_z^2) \quad (3.40)$$

where the integral is computed numerically since the expression of $f_y(y)$, given by (3.37), is complicated. In (3.40), R_{ca} is in [bits/channel use]. We can express this result in [nats/channel use] by changing the base of the logarithms from 2 to e .

In figure 3.3 the upper and lower bound along with the mutual information that approaches the channel capacity are plotted against the signal-to-noise ratio. It is evident that the capacity-approaching distribution has only two mass points in the low-SNR scenario, whereas the number of mass points increases in the high-SNR scenario.

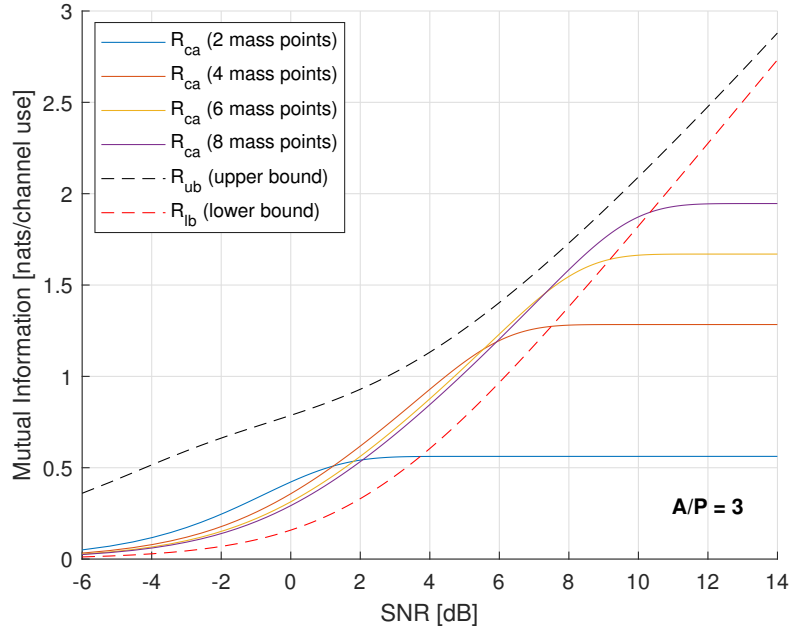


Figure 3.3: Upper and lower bounds on capacity along with the mutual information that approaches the capacity

Figure 3.4 illustrates the mutual information that approaches the channel capacity as a function of SNR, for different values of the peak-to-average ratio r . As can be seen, R_{ca} remains stable for $r \geq 6$. Practically, this case corresponds to the case of a dominant average power constraint over the peak power constraint.

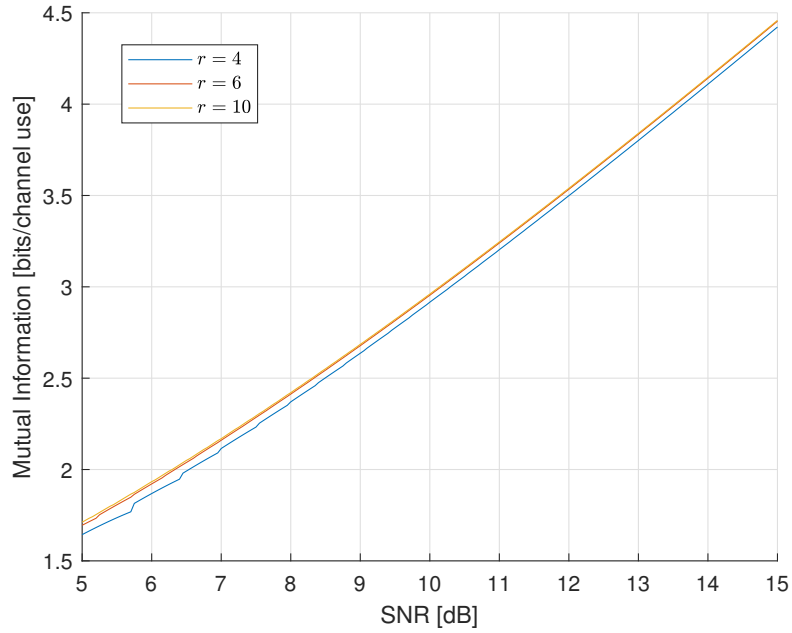


Figure 3.4: The mutual information that approaches the channel capacity versus SNR

3.2 Energy harvesting models

In chapter 2 as well as in most existing works regarding the rate-energy tradeoff analysis, the linear harvesting model was considered. In the linear model, the harvested energy (normalized by the symbol period) during the k th symbol interval is linearly proportional to the input power $\rho_k P_r$:

$$Q_L = \zeta \rho_k P_r \quad (3.41)$$

where $0 \leq \zeta \leq 1$ denotes the energy conversion efficiency, which is usually assumed to be constant, while P_r denotes the average received power, i.e, $P_r = \mathbb{E}[r(t)]$.

However, it has been shown experimentally that the practical energy harvesting circuits exhibit nonlinear behaviors, since the energy conversion efficiency varies over different power levels. In particular, the efficiency is improved when the input power increase to a certain level, but it is substantially degraded when the input power exceed a certain level. Additionally, the turn-on voltage and the reverse breakdown of the diode used in the rectifier circuit result in a small ζ at the low and high input power levels [37]. An increase in frequency also induces a decrease of the conversion efficiency [38]. Consequently, the linear model in (3.41) cannot capture the turn-on and saturation nonlinearities at the low and high input power levels, respectively, and thereby fails to accurately model the nonlinear behavior due to ideal and simplistic assumption of the constant efficiency.

To better match the experimental results of the practical EH circuits, a realistic nonlinear energy harvesting model based on the logistic (sigmoidal) function was proposed in [39]. In this nonlinear model, the harvested energy during the k th symbol interval is modeled as:

$$Q_{NL} = \frac{P_s(\Psi(\rho_k) - \Omega)}{1 - \Omega} \quad (3.42)$$

where Ω is a constant to ensure the zero-input zero-output response

$$\Omega = \frac{1}{1 + e^{AB}} \quad (3.43)$$

whereas $\Psi(\rho_k)$ is the logistic function, which takes the average power P_r as the input

$$\Psi(\rho_k) = \frac{1}{1 + e^{-A(\rho_k P_r - B)}} \quad (3.44)$$

Substituting (3.43) and (3.44) into (3.42), we have:

$$Q_{NL} = \frac{P_s}{e^{AB}} \left(\frac{1 + e^{AB}}{1 + e^{-A(\rho_k P_r - B)}} - 1 \right) \quad (3.45)$$

In (3.45), P_s denotes the maximum harvested power when the harvesting circuit is saturated, whereas A and B are positive constants related to the circuit specification. The parameters P_s , A and B are calculated by curve fitting.

For example, the authors in [40] derived the values of these parameters ($P_s = 0.024$, $A = 150$, $B = 0.014$) by fitting the nonlinear model given in (3.45) to the measurement data of the practical EH circuit (at 2.45GHz) suggested in [41]. The first graph of the figure 3.5 depicts the harvested energy using this nonlinear model over different input power levels. Using curve fitting to determine the energy conversion efficiency ζ of the linear model yields $\zeta = 0.78$. From

the second graph of the figure 3.5 it is evident that the linear EH model fails to accurately match the experimental results in low and high input power levels.

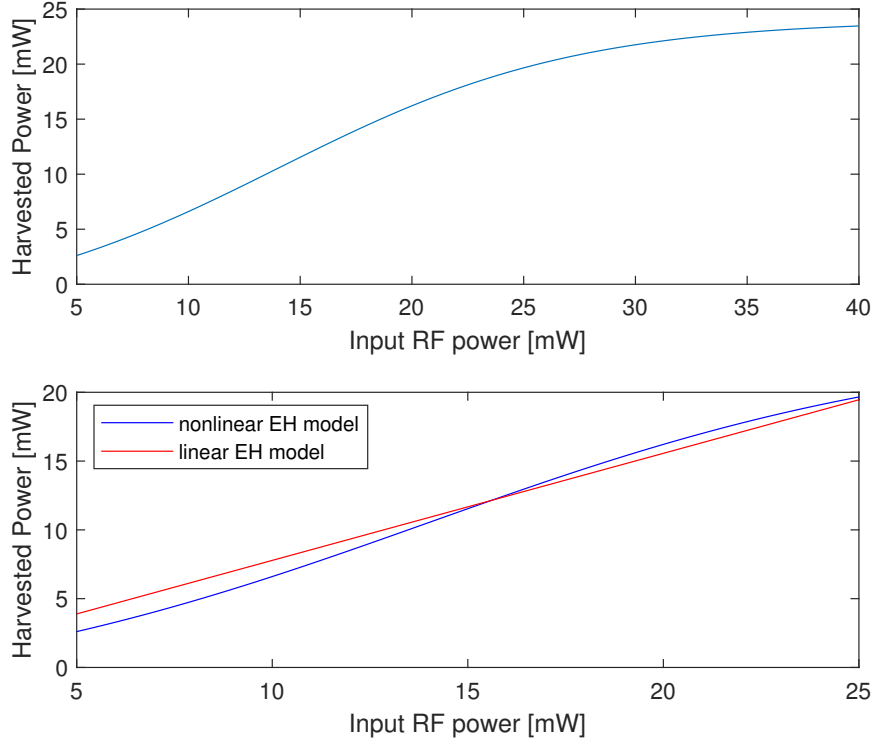


Figure 3.5: The nonlinear EH model (3.45) for $P_S = 0.024$, $A = 150$, $B = 0.014$ versus the average input power (the graph at the top of the figure). A comparison between the linear EH model with $\zeta = 0.78$ and the nonlinear EH model with $P_S = 0.024$, $A = 150$, $B = 0.014$ (the graph at the bottom of the figure).

3.3 System performance metrics

Having studied the capacity of the optical intensity channel as well as the energy stored in the battery, we can present the most commonly used metrics to evaluate the performance of the SWIPT system. To that end, the results of the first two sections should be adjusted to the system analyzed in chapter 1, for both PS and TS schemes described in (2.8) and (2.9), respectively.

Information Rate

Based on (3.17) and (3.40) and the minimum (capacity lower bound) and the maximum (capacity approaching) achievable rates of the channel (2.34):

- PS scheme

$$R_{lb,PS} = \frac{1}{2} \log_2 \left(1 + \frac{(v(r)hP)^2}{2\pi e\sigma_{z,PS}^2} \right) \quad (3.46)$$

$$R_{ca,PS} = R_{ca}(rhP, \sigma_{z,PS}^2) \quad (3.47)$$

where $h = Lh_{sum}$ and $\sigma_{z,PS}^2 = \sigma_{rec}^2 + \frac{\sigma_{ADC}^2}{(1-\rho)^2}$ due to (2.35) and (2.36), respectively.

- TS scheme

$$R_{lb,TS} = (1-a) \frac{1}{2} \log_2 \left(1 + \frac{(v(r)hP)^2}{2\pi e \sigma_{z,TS}^2} \right) \quad (3.48)$$

$$R_{ca,TS} = (1-a) R_{ca}(rhP, \sigma_{z,TS}^2) \quad (3.49)$$

where $h = Lh_{sum}$ and $\sigma_{z,TS}^2 = \sigma_{rec}^2 + \sigma_{ADC}^2$ due to (2.35 and (2.37), respectively.

Harvested Energy

In the first section, we deduced that the input distribution that achieves the minimum rate (3.11) as well as the input distribution that approaches the maximum achievable rate (3.27) have a mean value equal to \mathcal{E} , which is defined in (2.39). Hence, the average received power is derived from (2.22): $P_r = \mathbb{E}[i_{DC}(t)] = Lh_{sum}\mathcal{E}$, since the antenna noise can be ignored. Setting $P_r = Lh_{sum}\mathcal{E}$ in (3.41) and (3.45), we obtain:

- PS scheme

$$Q_{L,PS} = \rho \zeta h_{sum} L \mathcal{E} \quad (3.50)$$

$$Q_{NL,PS} = \frac{P_s}{e^{AB}} \left(\frac{1 + e^{AB}}{1 + e^{-A(\rho h_{sum} L \mathcal{E} - B)}} - 1 \right) \quad (3.51)$$

- TS scheme

$$Q_{L,TS} = a \zeta h_{sum} L \mathcal{E} \quad (3.52)$$

$$Q_{NL,TS} = a \frac{P_s}{e^{AB}} \left(\frac{1 + e^{AB}}{1 + e^{-A(h_{sum} L \mathcal{E} - B)}} - 1 \right) \quad (3.53)$$

3.3.1 Rate-Energy region

The information rate-harvested energy tradeoff is characterized by boundary of the rate-energy (R-E) region, which consists of all the achievable rate and energy pairs under given peak and average power constraints. The R-E region is defined as [13]:

- PS scheme

$$C_{R-E}^{PS}(P, rP) = \bigcup_{\rho \in [0,1]} \left\{ (R, Q) : Q \leq Q_{PS}, \quad R \leq R_{PS} \right\} \quad (3.54)$$

where Q_{PS} is given by (3.50) or (3.51), while R is given by (3.46) or (3.47).

- TS scheme

$$C_{R-E}^{TS}(P, rP) = \bigcup_{a \in [0,1]} \left\{ (R, Q) : Q \leq Q_{TS}, \quad R \leq R_{TS} \right\} \quad (3.55)$$

where Q_{TS} is given by (3.52) or (3.53), while R is given by (3.48) or (3.49).

3.3.2 Joint rate-energy outage probability

The aim of this subsection is to determine the optimal PS and TS factors, denoted as ρ^* and a^* respectively, by minimizing the maximum value of the outage probability, thereby specifying the optimal operating point in the determined R-E region. The analysis done in [14], where both the transmitter and the receiver are equipped with a single antenna, is thus generalized.

The joint rate-energy outage probability P_o is defined as the probability that the energy harvested by the receiver is lower than an energy threshold q_{th} , or the rate is lower than a rate threshold r_{th} . This definition can be expressed as:

$$P_o \triangleq \Pr(Q \leq q_{th} \cup R \leq r_{th}) \quad (3.56)$$

For a given energy harvesting model, the joint rate-energy outage probability in (3.56) attains its maximum value when the information rate attains its minimum value, that is, when $R = R_{lb}$, where R_{lb} is given by (3.17). For the sake of simplicity, in the sequel we will refer to this maximum value as outage probability. The outage probability will be minimized for PS and TS protocols regarding both EH models.

Proposition 3. *The outage probability for a MISO PS system is given by*

$$P_{o,PS} = \frac{1}{(n_T - 1)!} \gamma \left(n_T, \frac{1}{\sigma_h^2} \max \left\{ \frac{c_1}{\rho}, c_2 \sqrt{\sigma_{rec}^2 + \frac{\sigma_{ADC}^2}{(1-\rho)^2}} \right\} \right) \quad (3.57)$$

where the function $\gamma(s, x)$ is defined in (2.45), whereas the constants c_1, c_2 are equal to:

$$c_1 = \begin{cases} \frac{q_{th}}{\zeta L \mathcal{E}}, & \text{linear EH model} \\ \frac{1}{AL \mathcal{E}} \log \left(\frac{P_s + q_{th} e^{AB}}{P_s - q_{th}} \right), & \text{nonlinear EH model} \end{cases} \quad (3.58)$$

$$c_2 = \frac{1}{vLP} \sqrt{2\pi e (2^{2r_{th}} - 1)} \quad (3.59)$$

Proof. Firstly, we will solve the inequalities $R_{lb,PS} \leq r_{th}$, $Q_{L,PS} \leq q_{th}$ and $Q_{NL,PS} \leq q_{th}$ in terms of h_{sum} , regarding the PS scheme. The first two inequalities become:

$$\begin{aligned} R_{lb,PS} \leq r_{th} &\xrightarrow[(2.36)]{(3.46)} \frac{1}{2} \log_2 \left(1 + \frac{(vh_{sum}LP)^2}{2\pi e \left(\sigma_{rec}^2 + \frac{\sigma_{ADC}^2}{(1-\rho)^2} \right)} \right) \leq r_{th} \Rightarrow \frac{(vh_{sum}LP)^2}{2\pi e \left(\sigma_{rec}^2 + \frac{\sigma_{ADC}^2}{(1-\rho)^2} \right)} \leq 2^{2r_{th}} - 1 \\ \Rightarrow h_{sum} &\leq \frac{1}{vLP} \sqrt{2\pi e \left(\sigma_{rec}^2 + \frac{\sigma_{ADC}^2}{(1-\rho)^2} \right) (2^{2r_{th}} - 1)} \end{aligned} \quad (3.60)$$

and

$$Q_{L,PS} \leq q_{th} \xrightarrow{(3.50)} \rho \zeta h_{sum} L \mathcal{E} \leq q_{th} \Rightarrow h_{sum} \leq \frac{q_{th}}{\rho \zeta L \mathcal{E}} \quad (3.61)$$

Similarly, assuming $q_{th} < P_s$ and after some algebraic manipulation the inequality for the non-linear energy harvesting model yields

$$\begin{aligned} Q_{NL,PS} \leq q_{th} &\xrightarrow{(3.51)} \frac{P_s}{e^{AB}} \left(\frac{1 + e^{AB}}{1 + e^{-A(\rho h_{sum} L \mathcal{E} - B)}} - 1 \right) \leq q_{th} \\ \Rightarrow h_{sum} &\leq \frac{1}{\rho A L \mathcal{E}} \log \left(\frac{P_s + q_{th} e^{AB}}{P_s - q_{th}} \right) \end{aligned} \quad (3.62)$$

Regarding the linear EH model, the outage probability in (3.56) can be written as:

$$P_o = \Pr(Q_{L,PS} \leq q_{th} \cup R_{lb,PS} \leq r_{th})$$

Substituting (3.60) and (3.61) in the above expression we obtain:

$$P_o = \Pr \left(\left\{ h_{sum} \leq \frac{q_{th}}{\rho \zeta L \mathcal{E}} \right\} \cup \left\{ h_{sum} \leq \frac{1}{vLP} \sqrt{2\pi e \left(\sigma_{rec}^2 + \frac{\sigma_{ADC}^2}{(1-\rho)^2} \right) (2^{2r_{th}} - 1)} \right\} \right)$$

It can be observed that the random variable h_{sum} is upper-bounded in both events. The union of these events occurs when h_{sum} is lower than the minimum of these upper bounds. Hence, P_o can be expressed as

$$P_o = \Pr \left(h_{sum} \leq \max \left\{ \frac{q_{th}}{\rho \zeta L \mathcal{E}}, \frac{1}{vLP} \sqrt{2\pi e \left(\sigma_{rec}^2 + \frac{\sigma_{ADC}^2}{(1-\rho)^2} \right) (2^{2r_{th}} - 1)} \right\} \right)$$

With the aid of (2.48), the outage probability is given by:

$$P_o = \frac{1}{(n_T - 1)!} \gamma \left(n_T, \frac{1}{\sigma_h^2} \max \left\{ \frac{c_1}{\rho}, c_2 \sqrt{\sigma_{rec}^2 + \frac{\sigma_{ADC}^2}{(1-\rho)^2}} \right\} \right)$$

where

$$c_1 = \frac{q_{th}}{\zeta L \mathcal{E}}, \quad c_2 = \frac{1}{vLP} \sqrt{2\pi e (2^{2r_{th}} - 1)}$$

By substituting (3.60) and (3.62) into (3.56) and following the same procedure for the nonlinear EH model, the proof is completed. \square

The optimal PS factor ρ^* is obtained by minimizing the outage probability, i.e.:

$$\rho^* = \underset{\rho}{\operatorname{argmin}} P_o$$

Proposition 4. *The optimal value of $\rho \in (0, 1)$ is unique and is given by the solution of:*

$$\rho^4 - 2\rho^3 + \left(1 + \frac{\sigma_{ADC}^2}{\sigma_{rec}^2} - \frac{c_1^2}{c_2^2 \sigma_{rec}^2} \right) \rho^2 + \frac{2c_1^2}{c_2^2 \sigma_{rec}^2} \rho - \frac{c_1^2}{c_2^2 \sigma_{rec}^2} = 0 \quad (3.63)$$

where c_1 and c_2 are given by (3.58) and (3.59), respectively.

Proof. The function $\gamma(s, x)$ is an increasing function of x . Hence, from Proposition 3, it follows that minimizing P_o is equivalent to minimizing the maximum value

$$\max \left\{ \frac{c_1}{\rho}, c_2 \sqrt{\sigma_{rec}^2 + \frac{\sigma_{ADC}^2}{(1-\rho)^2}} \right\}$$

As the PS factor ρ increases, the first term in the above maximum value decreases, while the second increases. The probability is thus minimized when the above maximal value is minimized, that is the two terms are equal. Therefore, the optimal PS factor can be extracted from

$$\frac{c_1^2}{\rho^2} = c_2^2 \left(\sigma_{rec}^2 + \frac{\sigma_{ADC}^2}{(1-\rho)^2} \right)$$

Assuming

$$f(\rho) = \frac{c_1^2}{\rho^2} - c_2^2 \left(\sigma_{rec}^2 + \frac{\sigma_{ADC}^2}{(1-\rho)^2} \right), \quad \rho \in (0, 1)$$

We have $\lim_{\rho \rightarrow 0} f(\rho) = +\infty$ and $\lim_{\rho \rightarrow 1} f(\rho) = -\infty$, thus there is at least one root of $f(\rho)$ in $(0, 1)$. Moreover,

$$f'(\rho) = -\frac{2c_1^2}{\rho^3} - \frac{2\sigma_{ADC}^2}{(1-\rho)^3} < 0, \quad \rho \in (0, 1)$$

thus f is a decreasing function in $(0, 1)$ and the above root is unique. Solving the equation $f(\rho) = 0$, the equation (3.63) can easily be derived. \square

Proposition 5. *The outage probability for a MISO TS system is given by*

$$P_{o,TS} = \frac{1}{(n_T - 1)!} \gamma \left(n_T, \frac{1}{\sigma_h^2} \max\{c_1, c_2\} \right) \quad (3.64)$$

where the function $\gamma(s, x)$ is defined in (2.45), whereas the constants c_1, c_2 are equal to:

$$c_1 = \begin{cases} \frac{q_{th}}{a\zeta L\mathcal{E}}, & \text{linear EH model} \\ \frac{1}{AL\mathcal{E}} \log \left(\frac{aP_s + q_{th}e^{AB}}{aP_s - q_{th}} \right), & \text{nonlinear EH model} \end{cases} \quad (3.65)$$

$$c_2 = \frac{1}{vLP} \sqrt{2\pi e (\sigma_{rec}^2 + \sigma_{ADC}^2) \left(2^{\frac{2r_{th}}{1-a}} - 1 \right)} \quad (3.66)$$

For the nonlinear model the above expression holds when $a \in \left(\frac{q_{th}}{P_s}, 1 \right]$. If $a \in \left[0, \frac{q_{th}}{P_s} \right)$ outage always occurs.

Proof. Firstly, we will solve the inequalities $R_{lb,PS} \leq r_{th}$, $Q_{L,PS} \leq q_{th}$ and $Q_{NL,PS} \leq q_{th}$ in terms of h_{sum} , regarding the PS scheme. The first two inequalities become:

$$\begin{aligned} R_{lb,TS} \leq r_{th} &\xrightarrow[(2.37)]{(3.48)} \frac{1-a}{2} \log_2 \left(1 + \frac{(vh_{sum}LP)^2}{2\pi e (\sigma_{rec}^2 + \sigma_{ADC}^2)} \right) \leq r_{th} \Rightarrow \frac{(vh_{sum}LP)^2}{2\pi e (\sigma_{rec}^2 + \sigma_{ADC}^2)} \leq 2^{\frac{2r_{th}}{1-a}} - 1 \\ &\Rightarrow h_{sum} \leq \frac{1}{vLP} \sqrt{2\pi e (\sigma_{rec}^2 + \sigma_{ADC}^2) \left(2^{\frac{2r_{th}}{1-a}} - 1 \right)} \end{aligned} \quad (3.67)$$

and

$$Q_{L,TS} \leq q_{th} \xrightarrow{(3.52)} a\zeta h_{sum} L\mathcal{E} \leq q_{th} \Rightarrow h_{sum} \leq \frac{q_{th}}{a\zeta L\mathcal{E}} \quad (3.68)$$

Solving the inequality for the nonlinear energy harvesting model we obtain:

$$Q_{NL,TS} \leq q_{th} \xrightarrow{(3.53)} \frac{aP_s}{e^{AB}} \left(\frac{1 + e^{AB}}{1 + e^{-A(h_{sum}L\mathcal{E} - B)}} - 1 \right) \leq q_{th} \Rightarrow e^{-A(h_{sum}L\mathcal{E} - B)} \geq e^{AB} \frac{aP_s - q_{th}}{aP_s + q_{th}e^{AB}}$$

We observe that the last inequality (and thus the inequality $Q_{NL,TS} \leq q_{th}$) always holds when $a \leq q_{th}/P_s$. In the case where $a > q_{th}/P_s$, solving the above inequality in terms of h_{sum} yields:

$$h_{sum} \leq \frac{1}{AL\mathcal{E}} \log \left(\frac{aP_s + q_{th}e^{AB}}{aP_s - q_{th}} \right) \quad (3.69)$$

Regarding the linear EH model, the outage probability in (3.56) can be written as:

$$P_o = \Pr(Q_{L,TS} \leq q_{th} \cup R_{lb,TS} \leq r_{th})$$

Substituting (3.67) and (3.68) in the above expression we obtain:

$$P_o = \Pr \left(\left\{ h_{sum} \leq \frac{q_{th}}{a\zeta L\mathcal{E}} \right\} \cup \left\{ h_{sum} \leq \frac{1}{vLP} \sqrt{2\pi e (\sigma_{rec}^2 + \sigma_{ADC}^2) \left(2^{\frac{2r_{th}}{1-a}} - 1 \right)} \right\} \right)$$

It can be observed that the random variable h_{sum} is upper-bounded in both events. The union of these events occurs when h_{sum} is lower than the minimum of these upper bounds. Hence, P_o can be expressed as

$$P_o = \Pr \left(h_{sum} \leq \max \left\{ \frac{q_{th}}{a\zeta L\mathcal{E}}, \frac{1}{vLP} \sqrt{2\pi e (\sigma_{rec}^2 + \sigma_{ADC}^2) \left(2^{\frac{2r_{th}}{1-a}} - 1 \right)} \right\} \right)$$

With the aid of (2.48), the outage probability is given by:

$$P_o = \frac{1}{(n_T - 1)!} \gamma \left(n_T, \frac{1}{\sigma_h^2} \max \left\{ \frac{q_{th}}{a\zeta L\mathcal{E}}, \frac{1}{vLP} \sqrt{2\pi e (\sigma_{rec}^2 + \sigma_{ADC}^2) \left(2^{\frac{2r_{th}}{1-a}} - 1 \right)} \right\} \right)$$

By substituting (3.67) and (3.69) into (3.56) and following the same procedure for the nonlinear EH model, the proof is completed. \square

The optimal TS factor a^* is obtained by minimizing the outage probability, i.e.:

$$a^* = \underset{a}{\operatorname{argmin}} P_o$$

Proposition 6. *The optimal value of $a \in (0, 1)$ is unique and is given for the linear EH model by the solution of:*

$$a^2 \left(2^{\frac{2r_{th}}{1-a}} - 1 \right) - \frac{v^2 q_{th}^2 P^2}{2\pi e \zeta^2 \mathcal{E}^2 (\sigma_{rec}^2 + \sigma_{ADC}^2)} = 0 \quad (3.70)$$

and for the nonlinear EH model by the solution of

$$\left(2^{\frac{2r_{th}}{1-a}} - 1 \right) \log^{-2} \left(\frac{aP_s + q_{th}e^{AB}}{aP_s - q_{th}} \right) - \frac{v^2 P^2}{2\pi e A^2 \mathcal{E}^2 (\sigma_{rec}^2 + \sigma_{ADC}^2)} = 0 \quad (3.71)$$

Proof. The function $\gamma(s, x)$ is an increasing function of x . Hence, from Proposition 5, it follows that minimizing P_o for the linear EH model is equivalent to minimizing the maximum value

$$\max \left\{ \frac{q_{th}}{a\zeta L\mathcal{E}}, \frac{1}{vLP} \sqrt{2\pi e (\sigma_{rec}^2 + \sigma_{ADC}^2) \left(2^{\frac{2r_{th}}{1-a}} - 1 \right)} \right\}$$

As the TS factor a increases, the first term in the above maximum value decreases, while the second increases. The probability is thus minimized when the above maximal value is minimized, that is, the two terms are equal. Therefore, the optimal PS factor can be extracted from

$$\left(\frac{q_{th}}{a\zeta L\mathcal{E}} \right)^2 = \left(\frac{1}{vLP} \right)^2 2\pi e (\sigma_{rec}^2 + \sigma_{ADC}^2) \left(2^{\frac{2r_{th}}{1-a}} - 1 \right)$$

Assuming

$$f(a) = \left(\frac{q_{th}}{a\zeta L\mathcal{E}} \right)^2 - \left(\frac{1}{vLP} \right)^2 2\pi e (\sigma_{rec}^2 + \sigma_{ADC}^2) \left(2^{\frac{2r_{th}}{1-a}} - 1 \right), \quad a \in (0, 1)$$

We have $\lim_{a \rightarrow 0} f(a) = +\infty$ and $\lim_{a \rightarrow 1} f(a) = -\infty$, thus there is at least one root of $f(a)$ in $(0, 1)$. Moreover,

$$f'(a) = -\frac{2}{a^3} \left(\frac{q_{th}}{\zeta L \mathcal{E}} \right)^2 - \left(\frac{1}{vLP} \right)^2 2\pi e (\sigma_{rec}^2 + \sigma_{ADC}^2) r_{th} \log(2) \frac{2^{\frac{2r_{th}}{1-a}+1}}{(1-a)^2} < 0, \quad a \in (0, 1)$$

thus f is a decreasing function in $(0, 1)$ and the above root is unique. Solving the equation $f(a) = 0$, the equation (3.70) can easily be derived. To complete the proof, we need to follow the same procedure for the nonlinear EH model, that is, we should minimize the quantity $\max\{c_1, c_2\}$, where c_1, c_2 are given by (3.65) and (3.66), respectively. \square

Chapter 4

Numerical results and discussion

In this chapter the obtained simulation results are used to quantify the performance of the system and can be viewed as the benchmark for further discussion.

4.1 Simulations

As far as the numerical data used for the following simulations is concerned, we assume that the receiver is a small sensor with aperture $a_r = 0.01m$. We set the aperture of the transmitter $a_t = 0.5m$ and the carrier frequency $f_c = 2.45GHz$. Moreover, without loss of generality and unless stated otherwise, it is assumed that $P = 2W$, $r = 3$, $d = 12m$, $q_{th} = 0.1mJ$, $r_{th} = 0.1bits/channel\ use$, $\sigma_{rec}^2 = \sigma_{ADC}^2 = \sigma^2$, where $LP/\sigma = 10dB$, and $h_i \sim \mathcal{CN}(0, 1)$, $i \in \{1, \dots, n_T\}$. We should also mention that the nonlinear EH model presented in section 3.2 is considered in all figures regarding the harvested energy. In order to avoid confusion between the peak power constraint A and the constant A of the nonlinear EH model, the peak power constraint was substituted by its equivalent term rP , as a result of (3.2)

• Simulation 1: R-E region

Firstly, in figures 4.1 and 4.2 the achievable rate-energy region is plotted against the number of the transmitter's antennas for the PS and TS protocols, respectively. In these simulations 10^4 channel realizations (h_{sum}) were considered. In both figures the dashed lines correspond to the minimum rate, while the solid line correspond to the capacity approaching rate.

As expected, the increase of the transmitter's antennas n_T enlarges the R-E region for both schemes. In particular, doubling the n_T results in a twofold increase of the maximum harvested energy (we set $\rho = 1$ and $a = 1$ for PS and TS respectively), while the maximum achievable rate (we set $\rho = 0$ and $a = 0$ for PS and TS respectively) increases by $1bit/channel\ use$. The increase of SNR (as a result of the increase of n_T) decreases the gap between R_{lb} and R_{ca} since the lower and upper bounds are identical in the high-SNR scenario, according to Chapter 2. Consequently, the gap between the curves (R_{lb}, Q_{NL}) and (R_{ca}, Q_{NL}) shrinks as the number of the transmitter's antennas increases. Therefore, the higher the ratio LP/σ the smaller the gap between the R-E regions achieved by the minimum R_{lb} and the maximum rate R_{ca} (assuming that n_T remains constant).

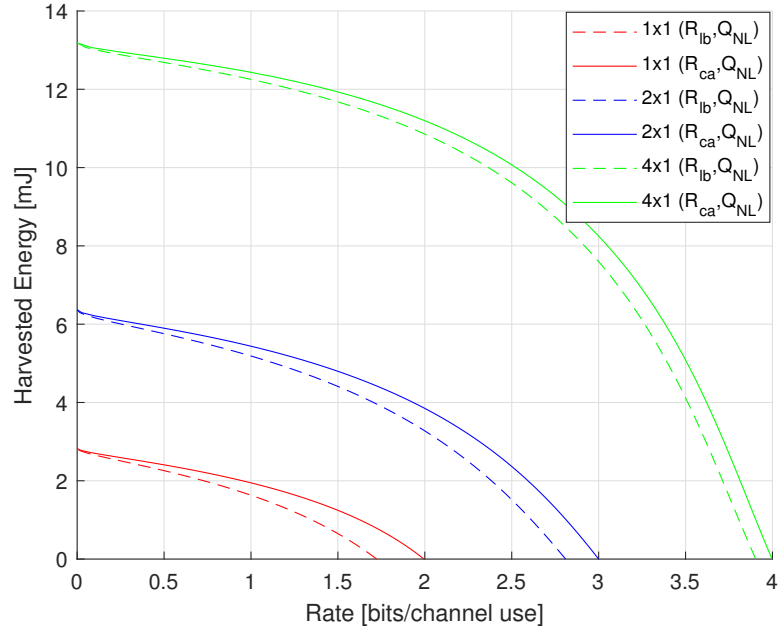


Figure 4.1: Rate-energy tradeoff in a $n_T \times 1$ MISO PS system, where $n_T = 1, 2, 4$.

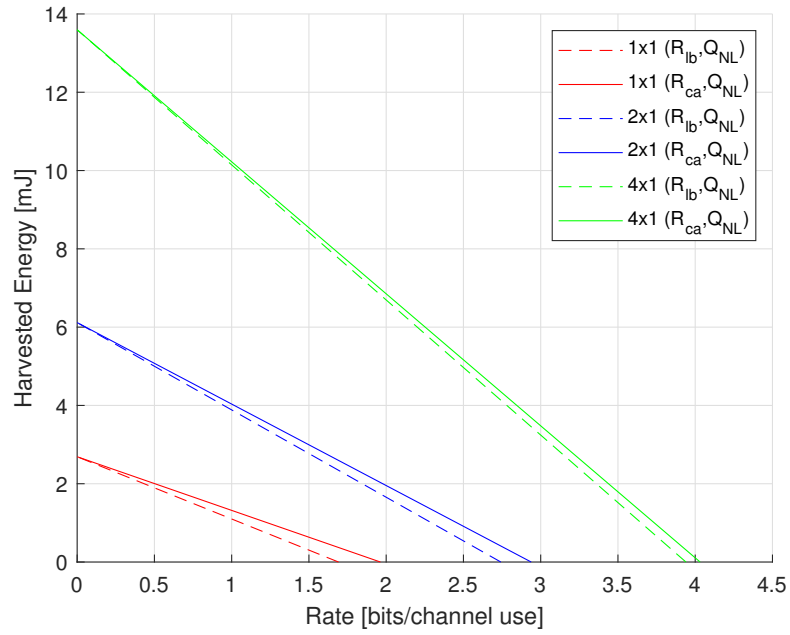


Figure 4.2: Rate-energy tradeoff in a $n_T \times 1$ MISO TS system, where $n_T = 1, 2, 4$.

In figure 4.3 the achievable R-E regions of PS and TS protocols are compared for two different values of the ratio LP/σ , in the case where the transmitter is equipped with only one antenna. As it can be observed, C_{R-E}^{TS} is greater than C_{R-E}^{PS} when $R_{ca} \in [0, r_{ca}]$, where r_{ca} increases as the ratio LP/σ decreases. Hence, the TS scheme is used to harvest greater amount of energy in the low-SNR scenario where the rate is small. However, PS outperforms TS in the high-SNR scenario.

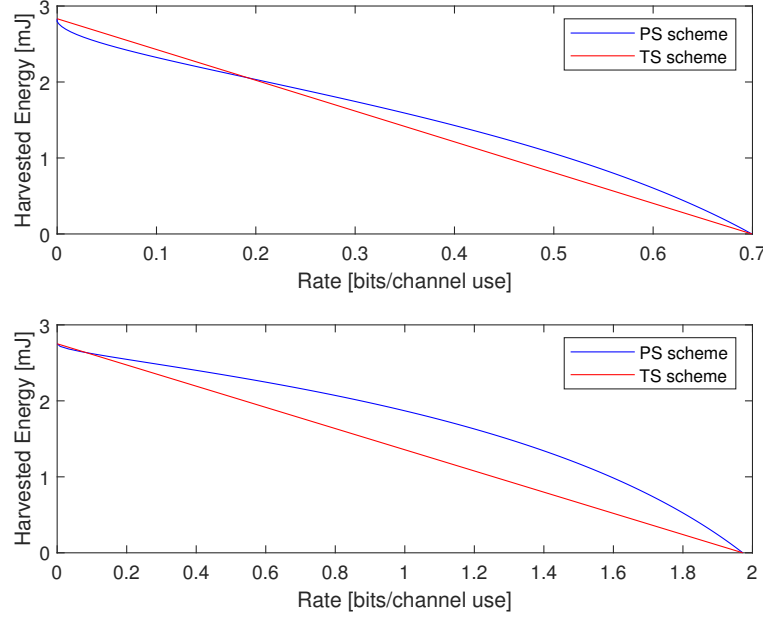


Figure 4.3: A comparison between the R-E regions of the PS and TS schemes for $\frac{LP}{\sigma} = 3 \text{ dB}$ (the graph at the top of the figure) and $\frac{LP}{\sigma} = 10 \text{ dB}$ (the graph at the bottom of the figure), where $n_T = 1$.

• Simulation 2: Optimal splitting factors

In order for the outage probability to be computed, the optimal splitting factors need first to be determined based on (3.63) and (3.71). From these expressions it can be easily deduced that the optimal splitting factors are independent of two main system parameters, namely, the number of the antennas n_T of the transmitter and the distance d between the base station and the receiver. However they depend on the energy threshold q_{th} , the rate threshold r_{th} and the ratio r between peak and average power constraints via the quantity $\frac{v^2 P^2}{\mathcal{E}^2}$, where v and \mathcal{E} are given in (3.18) and (2.39), respectively.

In figure 4.4 we can observe how the optimal PS factor ρ^* and optimal TS factor a^* vary over different values of r . It is evident that the shape of the graph is quite similar for both schemes, which can be explained by making use of the definitions of v , \mathcal{E} . In particular, when $r \leq 2$, $v = r$ and thus $\mathcal{E} = \frac{A}{2} = \frac{rP}{2}$ resulting in $\frac{v^2 P^2}{\mathcal{E}^2} = 4$. Consequently, ρ^* and a^* remain stable when $r \in [1, 2]$. In the case where $r > 2$, we have $\mathcal{E} = P$ resulting in $\frac{v^2 P^2}{\mathcal{E}^2} = v^2$, which means that the value of the optimal splitting factors increases as the ratio r increases. This is a quite reasonable conclusion since the increase of r leads to a higher information rate. Hence to assure that $R \geq r_{th}$, we need not increase the proportion $1 - \rho^*$ of the power of the received signal or the proportion $1 - a^*$ of the transmission time used for the decoding process. The proportion

(ρ^* for PS and a^* for TS) of the harvested energy can thus increase.

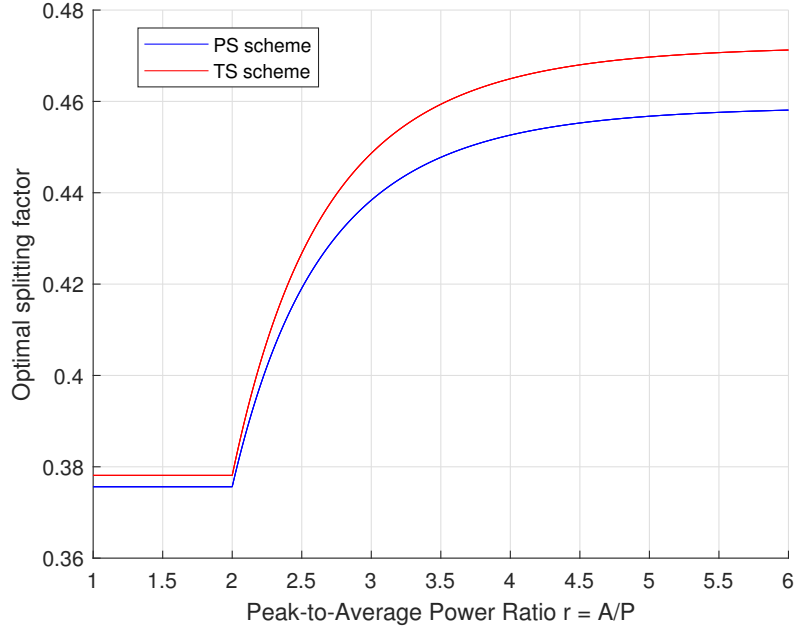
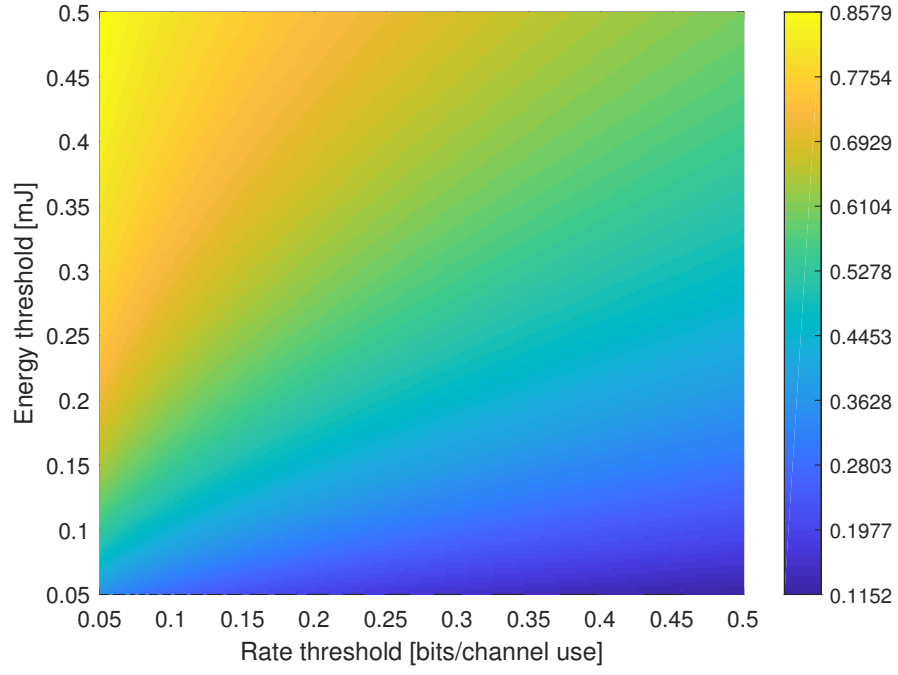
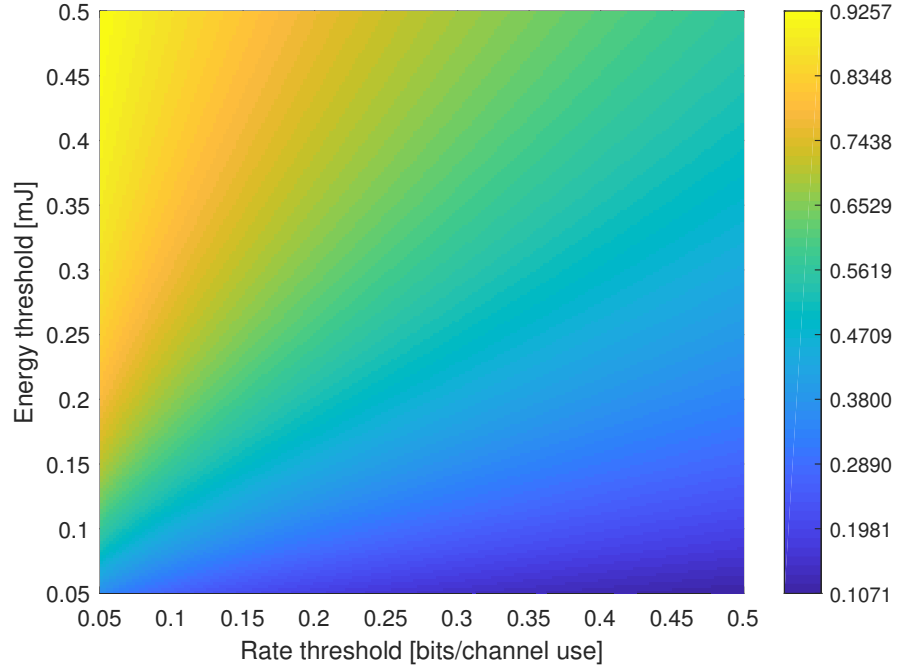


Figure 4.4: Optimal splitting factors ρ^* (PS scheme), a^* (TS scheme) versus the peak-to-average power ratio r .

Figures 4.5 and 4.6 illustrate the effect of both thresholds for harvested energy and achievable rate on the optimal selection of ρ and a . It is evident that both ρ^* and a^* increase when the energy (which is related to ρ for PS or a for TS) threshold increases or the rate (which is related to $1 - \rho$ for PS or $1 - a$ for TS) threshold decreases. As far as the PS scheme is concerned, we should mention that $\rho^* \in (0, 1)$ spans a large range of values for different thresholds. This is an interesting observation and highlights the importance of the ADC noise, since when this is ignored ($\sigma_{ADC} \rightarrow 0$ in (2.32)), the factor $1 - \rho$ does not affect the SNR at the receiver as it alters both signal and noise power equally. We can thus choose $\rho^* \rightarrow 1$ maximizing the harvested energy, since the achievable rate is independent of the PS factor. In this case only a small portion of the received signal is used for decoding, with the result that the ADC becomes comparable to the signal power, which is likely to have a destructive impact to the achievable quality of communication.

Figure 4.5: Optimal PS factor ρ^* versus energy and rate thresholds.Figure 4.6: Optimal TS factor a^* versus energy and rate thresholds.

• **Simulation 3: Outage probability**

After the optimal splitting factors have been identified, the outage probability is computed based on (3.57) and (3.64) for PS and TS protocols, respectively. The following figures depict the behaviour of the outage probability in some hypothetical scenarios.

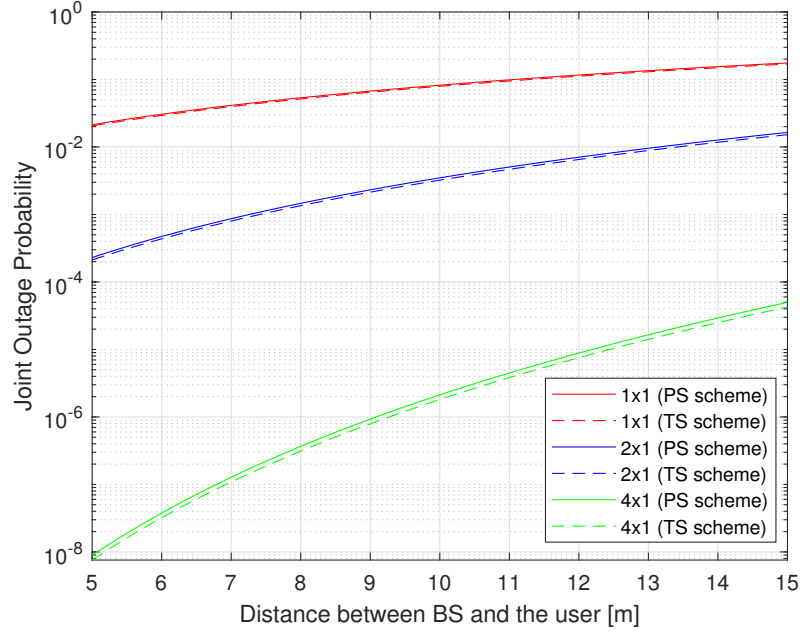


Figure 4.7: Outage probability versus BS-receiver distance for PS and TS schemes in a $n_T \times 1$ MISO system, where $n_T \in \{1, 2, 4\}$.

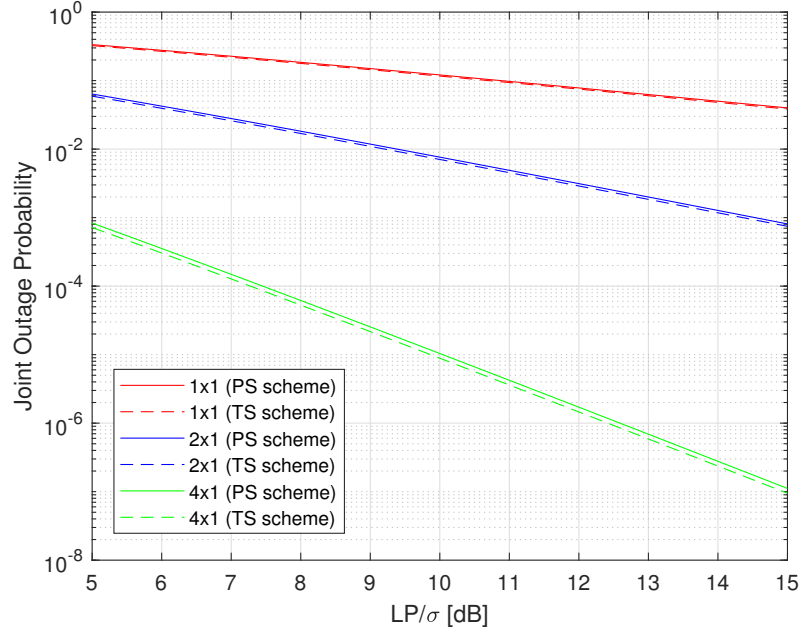


Figure 4.8: Outage probability versus LP/σ for PS and TS schemes in a $n_T \times 1$ MISO system, where $n_T \in \{1, 2, 4\}$.

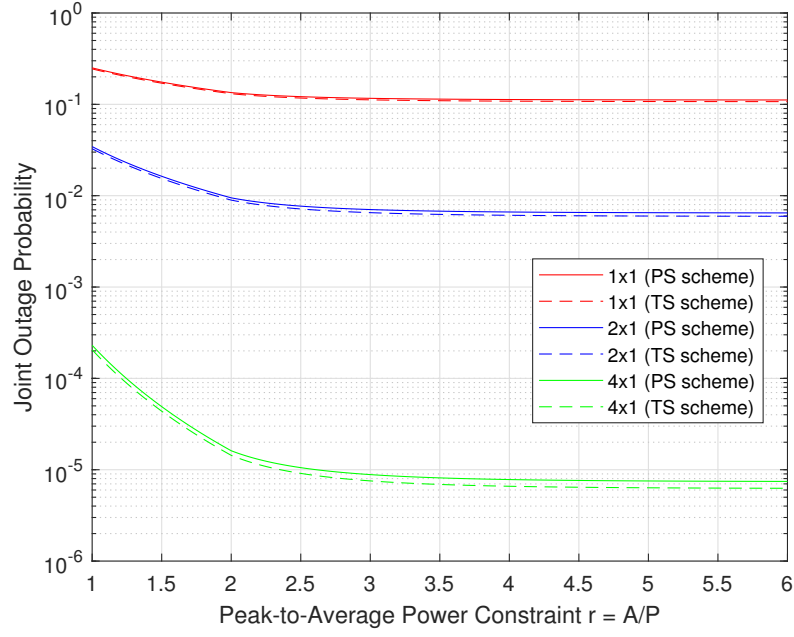


Figure 4.9: Outage probability versus r for PS and TS schemes in a $n_T \times 1$ MISO system, where $n_T \in \{1, 2, 4\}$.

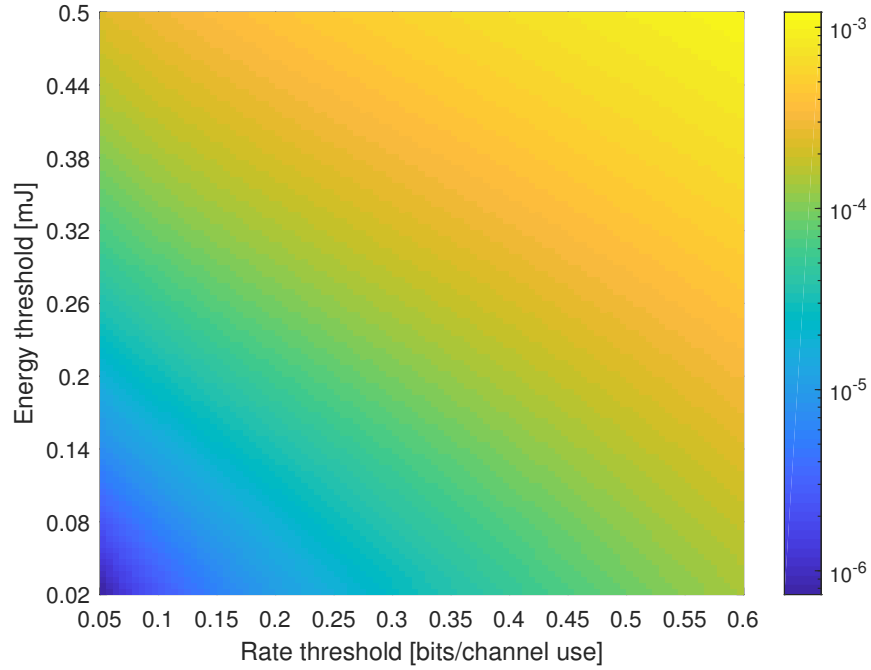


Figure 4.10: Outage probability versus r_{th} and q_{th} for PS scheme, where the BS has $n_T = 4$ antennas.

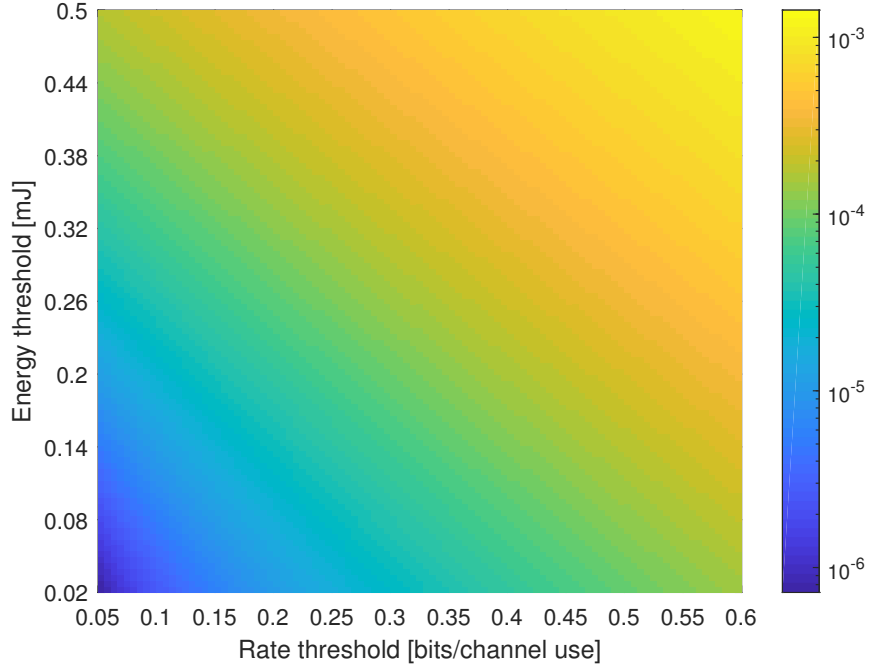


Figure 4.11: Outage probability versus r_{th} and q_{th} for TS scheme, where the BS has $n_T = 4$ antennas.

From the first three figures (fig. 4.7-4.9) it can be inferred that the greater the distance between the transmitter-receiver distance and the smaller the ratios r , LP/σ , the greater the outage probability. However, P_o decrease dramatically by doubling the number of the transmitter's antennas.

These figures also reveal that $P_{0,TS} < P_{0,PS}$ in most cases. However, this conclusion is not universal since it depends on the value of r_{th} , q_{th} , LP/σ . More specifically, simulations showed that increasing LP/σ or r_{th} , or decreasing q_{th} , result in $P_{0,TS} > P_{0,PS}$. Additionally, P_o reaches a plateau when $r \geq 3$ (fig. 4.9).

The last two figures (fig. 4.10 and 4.11) assert that the outage probability increases when either the energy of the rate threshold increases. In case four antennas are used in the base station, the outage probability is no greater than 10^{-3} for $q_{th} \leq 0.5 \text{ mJ}$ and $r_{th} \leq 0.5 \text{ bits/channel use}$. the results are similar for both PS and TS schemes.

4.2 Conclusions

Although the tight time constraints a thesis do not facilitate a thorough analysis of a specific topic, this thesis summarized and further analyzed the recent research findings in the area of Simultaneous Wireless Information and Power Transfer. Since Wireless Power Transfer constitutes and indispensable part of 5G Networks, the field has become quite interesting since it has drawn the attention of many researchers and has led to a noticeable progress. Subsequently, this thesis is considered the onset of further study and analysis of the SWIPT systems.

Some topics that have not been covered and need further investigation are the following. First, in case the receiver antenna noise is taken into account, the capacity analysis of the

channel is definitely more challenging. Second, it has not been proved that beamforming on the transmitter's side, which maximizes that receiver's harvested energy, maximizes the mutual information as well. The analysis becomes even more complex in MIMO systems with one or more end users, where the same or different information is sent to each user, since there is not a closed-form expression for the capacity of the optical channels. Hence, many advancements in the area Information Theory should forego a more thorough analysis of the integrated receiver.

References

- [1] A. M. Zungeru, L.-M. Ang, S. Prabakaran, and K. P. Seng, “Radio frequency energy harvesting and management for wireless sensor networks,” in *Green mobile devices and networks: Energy optimization and scavenging techniques*. CRC Press New York, NY, USA, 2012, no. 13, pp. 341–368.
- [2] L. R. Varshney, “Transporting information and energy simultaneously,” in *2008 IEEE International Symposium on Information Theory*. IEEE, 2008, pp. 1612–1616.
- [3] P. Grover and A. Sahai, “Shannon meets tesla: Wireless information and power transfer,” in *2010 IEEE international symposium on information theory*. IEEE, 2010, pp. 2363–2367.
- [4] A. M. Fouladgar and O. Simeone, “On the transfer of information and energy in multi-user systems,” *IEEE Communications Letters*, vol. 16, no. 11, pp. 1733–1736, 2012.
- [5] I. Krikidis, S. Timotheou, S. Nikolaou, G. Zheng, D. W. K. Ng, and R. Schober, “Simultaneous wireless information and power transfer in modern communication systems,” *IEEE Communications Magazine*, vol. 52, no. 11, pp. 104–110, 2014.
- [6] L. Liu, R. Zhang, and K.-C. Chua, “Wireless information transfer with opportunistic energy harvesting,” *IEEE Transactions on Wireless Communications*, vol. 12, no. 1, pp. 288–300, 2012.
- [7] R. Zhang and C. K. Ho, “MIMO broadcasting for simultaneous wireless information and power transfer,” *IEEE Transactions on Wireless Communications*, vol. 12, no. 5, pp. 1989–2001, 2013.
- [8] Z. Xiang and M. Tao, “Robust beamforming for wireless information and power transmission,” *IEEE Wireless Communications Letters*, vol. 1, no. 4, pp. 372–375, 2012.
- [9] K. Xiong, B. Wang, and K. R. Liu, “Rate-energy region of SWIPT for MIMO broadcasting under nonlinear energy harvesting model,” *IEEE Transactions on Wireless Communications*, vol. 16, no. 8, pp. 5147–5161, 2017.
- [10] X. Chen, Z. Zhang, H.-H. Chen, and H. Zhang, “Enhancing wireless information and power transfer by exploiting multi-antenna techniques,” *IEEE Communications Magazine*, vol. 53, no. 4, pp. 133–141, 2015.

- [11] Z. Ding, C. Zhong, D. W. K. Ng, M. Peng, H. A. Suraweera, R. Schober, and H. V. Poor, "Application of smart antenna technologies in simultaneous wireless information and power transfer," *IEEE Communications Magazine*, vol. 53, no. 4, pp. 86–93, 2015.
- [12] X. Chen, X. Wang, and X. Chen, "Energy-efficient optimization for wireless information and power transfer in large-scale MIMO systems employing energy beamforming," *IEEE Wireless Communications Letters*, vol. 2, no. 6, pp. 667–670, 2013.
- [13] X. Zhou, R. Zhang, and C. K. Ho, "Wireless information and power transfer: Architecture design and rate-energy tradeoff," *IEEE Transactions on communications*, vol. 61, no. 11, pp. 4754–4767, 2013.
- [14] S. A. Tegos, P. D. Diamantoulakis, K. N. Pappi, P. C. Sofotasios, S. Muhaidat, and G. K. Karagiannidis, "Toward efficient integration of information and energy reception," *IEEE Transactions on Communications*, vol. 67, no. 9, pp. 6572–6585, 2019.
- [15] E. Goudeli, C. Psomas, and I. Krikidis, "An integrated SWIPT receiver using non-coherent detection schemes," in *2018 IEEE Global Communications Conference (GLOBECOM)*, 2018, pp. 1–7.
- [16] Q. Shi, L. Liu, W. Xu, and R. Zhang, "Joint transmit beamforming and receive power splitting for MISO SWIPT systems," *IEEE Transactions on Wireless Communications*, vol. 13, no. 6, pp. 3269–3280, 2014.
- [17] J. Xu, L. Liu, and R. Zhang, "Multiuser MISO beamforming for simultaneous wireless information and power transfer," *IEEE Transactions on Signal Processing*, vol. 62, no. 18, pp. 4798–4810, 2014.
- [18] M. R. Khandaker and K.-K. Wong, "SWIPT in MISO multicasting systems," *IEEE Wireless Communications Letters*, vol. 3, no. 3, pp. 277–280, 2014.
- [19] M. Ju and H.-C. Yang, "Rate-energy outage analysis of MISO SWIPT with multiple energy harvesting sensors," *IEEE Access*, vol. 7, pp. 177 187–177 197, 2019.
- [20] K. Huang and E. Larsson, "Simultaneous information and power transfer for broadband wireless systems," *IEEE Transactions on Signal Processing*, vol. 61, no. 23, pp. 5972–5986, 2013.
- [21] D. W. K. Ng, E. S. Lo, and R. Schober, "Wireless information and power transfer: Energy efficiency optimization in OFDMA systems," *IEEE Transactions on Wireless Communications*, vol. 12, no. 12, pp. 6352–6370, 2013.
- [22] X. Zhou, R. Zhang, and C. K. Ho, "Wireless information and power transfer in multiuser OFDM systems," *IEEE Transactions on Wireless Communications*, vol. 13, no. 4, pp. 2282–2294, 2014.
- [23] Y. Liu, Z. Ding, M. El Kashlan, and H. V. Poor, "Cooperative non-orthogonal multiple access with simultaneous wireless information and power transfer," *IEEE Journal on Selected Areas in Communications*, vol. 34, no. 4, pp. 938–953, 2016.

- [24] P. D. Diamantoulakis, K. N. Pappi, Z. Ding, and G. K. Karagiannidis, “Wireless-powered communications with non-orthogonal multiple access,” *IEEE Transactions on Wireless Communications*, vol. 15, no. 12, pp. 8422–8436, 2016.
- [25] C. Zhong, H. A. Suraweera, G. Zheng, I. Krikidis, and Z. Zhang, “Wireless information and power transfer with full duplex relaying,” *IEEE Transactions on Communications*, vol. 62, no. 10, pp. 3447–3461, 2014.
- [26] Z. Ding, S. M. Perlaza, I. Esnaola, and H. V. Poor, “Power allocation strategies in energy harvesting wireless cooperative networks,” *IEEE Transactions on Wireless Communications*, vol. 13, no. 2, pp. 846–860, 2014.
- [27] I. Krikidis, “Simultaneous information and energy transfer in large-scale networks with/without relaying,” *IEEE Transactions on Communications*, vol. 62, no. 3, pp. 900–912, 2014.
- [28] P. D. Diamantoulakis, G. D. Ntouni, K. N. Pappi, G. K. Karagiannidis, and B. S. Sharif, “Throughput maximization in multicarrier wireless powered relaying networks,” *IEEE Wireless Communications Letters*, vol. 4, no. 4, pp. 385–388, 2015.
- [29] H. Ju and R. Zhang, “Throughput maximization in wireless powered communication networks,” *IEEE Transactions on Wireless Communications*, vol. 13, no. 1, pp. 418–428, 2013.
- [30] A. Lapidoth, S. M. Moser, and M. A. Wigger, “On the capacity of free-space optical intensity channels,” *IEEE Transactions on Information Theory*, vol. 55, no. 10, pp. 4449–4461, 2009.
- [31] K. Huang and X. Zhou, “Cutting the last wires for mobile communications by microwave power transfer,” *IEEE Communications Magazine*, vol. 53, no. 6, pp. 86–93, 2015.
- [32] C. A. Coelho, “The generalized integer gamma distribution—a basis for distributions in multivariate statistics,” *Journal of Multivariate Analysis*, vol. 64, no. 1, pp. 86–102, 1998.
- [33] T. M. Cover and J. A. Thomas, “Elements of information theory (wiley series in telecommunications and signal processing),” 2006.
- [34] S. Hranilovic and F. R. Kschischang, “Capacity bounds for power-and band-limited optical intensity channels corrupted by gaussian noise,” *IEEE Transactions on Information Theory*, vol. 50, no. 5, pp. 784–795, 2004.
- [35] J. G. Smith, “The information capacity of amplitude-and variance-constrained scalar gaussian channels,” *Information and control*, vol. 18, no. 3, pp. 203–219, 1971.
- [36] A. A. Farid and S. Hranilovic, “Channel capacity and non-uniform signalling for free-space optical intensity channels,” *IEEE Journal on Selected Areas in Communications*, vol. 27, no. 9, pp. 1553–1563, 2009.
- [37] J. Kang, I. Kim, and D. I. Kim, “Wireless information and power transfer: Rate-energy tradeoff for nonlinear energy harvesting,” *IEEE Transactions on Wireless Communications*, vol. 17, no. 3, pp. 1966–1981, 2018.

- [38] C. R. Valenta and G. D. Durgin, “Harvesting wireless power: Survey of energy-harvester conversion efficiency in far-field, wireless power transfer systems,” *IEEE Microwave Magazine*, vol. 15, no. 4, pp. 108–120, 2014.
- [39] E. Boshkovska, D. W. K. Ng, N. Zlatanov, and R. Schober, “Practical non-linear energy harvesting model and resource allocation for SWIPT systems,” *IEEE Communications Letters*, vol. 19, no. 12, pp. 2082–2085, 2015.
- [40] E. Boshkovska, N. Zlatanov, L. Dai, D. W. K. Ng, and R. Schober, “Secure SWIPT networks based on a non-linear energy harvesting model,” in *2017 IEEE Wireless Communications and Networking Conference Workshops (WCNCW)*, 2017, pp. 1–6.
- [41] Jiapin Guo and Xinen Zhu, “An improved analytical model for RF-DC conversion efficiency in microwave rectifiers,” in *2012 IEEE/MTT-S International Microwave Symposium Digest*, 2012, pp. 1–3.